MDPI

*Review*

# Perturbation-Based Battery Impedance Characterization Methods: From the Laboratory to Practical Implementation

Chuanxin Fan [1],*, Xinxiang Tian [2] and Chunfei Gu [2]

[1] School of Automation, Nanjing Institute of Technology, Nanjing 211167, China
[2] School of Electrical Power Engineering, Nanjing Institute of Technology, Nanjing 211167, China; y00450230530@njit.edu.com (X.T.); chunfei.gu@njit.edu.cn (C.G.)
* Correspondence: chuanxin.fan@njit.edu.cn

**Abstract:** To guarantee the secure and effective long-term functionality of lithium-ion batteries, vital functions, including lifespan estimation, condition assessment, and fault identification within battery management systems, are necessary. Battery impedance is a crucial indicator for assessing battery health and longevity, serving as an important reference in battery state evaluation. This study offers a comprehensive review of the characterization and applications of impedance spectroscopy. It highlights the increasing attention paid to broadband perturbation signals for impedance measurements, which promotes impedance characterization methods from laboratory to practical implementation. The impact of varying impedance characteristics on distinct cell states and their utilization is further examined. The discussion encompasses the challenges and opportunities for future research on onboard battery management system characterizations.

**Keywords:** lithium-ion battery; perturbation signal; multi-sine signal; electrochemical impedance spectroscopy; battery modeling

## 1. Introduction

To reduce climate pollution, countries have commenced the gradual establishment of new power systems reliant on renewable energy sources. As a fundamental component of the new energy sector, the advancement of energy storage technology has garnered significant attention. Among various energy storage batteries, the lithium-ion battery (LIB) has emerged as the predominant energy storage solution due to its minimal self-discharge rate, elevated energy density, extended cycle life, and absence of memory effect [1,2]. To ensure LIB's safety and power performance, it is essential to develop key functions in battery management systems, including health prediction, state estimation, fault diagnosis, and early warning systems for energy storage [3]. The state of health (SOH) and state of charge (SOC) of lithium-ion batteries facilitate precise estimations that enhance battery longevity and safety. Additionally, battery fault diagnosis ensures the secure and dependable operation of the energy storage system, optimizes its stable usage, and establishes a foundation for energy and safety management within the system [4,5]. The impedance of a LIB is influenced by its state, making it a critical parameter for monitoring and controlling the battery. Compared to other metrics such as current and voltage, impedance provides a more precise characterization of the battery's operational condition and longevity. Consequently, research on impedance measurement has garnered significant interest [6–8].

Several review papers have been published so far, focusing on the widely known battery electrochemical impedance spectroscopy (EIS) test and related applications. For example, Osaka et al. summarized an overview of diagnostic techniques for determining the health status of commercial LIBs using electrochemical impedance energy spectroscopy using equivalent circuit design techniques and also proposed the use of square-wave current signals for monitoring large-scale LIB systems, enabling the development of techniques for large-scale monitoring of lithium batteries [9]. Carthy et al. provide

a comprehensive analysis of the many uses of battery impedance spectra in the assessment of battery SOC, SOH, and internal temperature and have conducted in-depth analyses of the partial impedance of batteries, internal chemical mechanisms, battery models, and the accuracy of each model, demonstrating that impedance is affected by multiple factors, but fault detection for batteries is rarely mentioned [10]. Sun et al. and Liu et al. review the EIS method for battery health-state estimation and LIB aging mechanism analysis. The former established the relationship between characteristic parameters and SOH by constructing a frequency-domain equivalent circuit model and used a data-driven method to construct the relationship between EIS data and SOH, which provided a new way of thinking about SOH prediction based on EIS, and the latter classified the EIS according to different principles. The latter classifies EIS measurements according to different principles, analyses the connection between aging and SOH in lithium batteries, proves that impedance-based SOH prediction is more accurate than the traditional technique, and deepens the researchers' understanding of impedance spectra [11,12]. These reviews have focused primarily on the conventional EIS test for impedance measurement and various impedance applications for battery condition assessment. However, the existing EIS technique is notably laborious and challenging to perform on onboard applications. To push the impedance characterization methods from laboratory to practical implementation, this paper mainly reviews the novel perturbation signals employed in extracting the impedance response of a LIB and highlights their potential in capturing and analyzing the battery's in-depth characters. From the perspective of impedance applications, we believe that this study will contribute to the development of the next generation of advanced battery management systems (BMS).

The impedance measurement of lithium-ion batteries can be obtained by several methodologies owing to the variability of testing conditions, operational settings, and excitation signals. This paper aims to systematically analyze and summarize the perturbation signals for LIB characterization, examining the methods and applications for assessing the battery impedance. It will address the types of signals, their applications, strengths and weaknesses, improvement strategies, and the challenges and future obstacles encountered by current impedance measurement methods in detail.

The primary contributions of this paper are enumerated as follows:

- The classification of perturbation signals for battery impedance characterization is established, and the content of this classification, such as sine-sweep signal, step signal, square wave signal, pseudo-random binary sequences, and multisine signals, is systematically reviewed.
- The fundamental elements of perturbation signal design and their respective functions in battery impedance characterization are outlined, along with the advantages and limits of these perturbation signals for potential enhancement.
- This study examines the factors affecting the impedance of Li-ion batteries, such as remaining battery life, state of charge, and variation in internal electrochemical processes, to facilitate the application of battery impedance for predicting battery life, fault detection, state of charge estimation, and battery modeling.

The primary contents of the paper are organized as follows. Section 2 outlines the fundamental theory of the battery impedance spectrum. Section 3 presents the classification of perturbation signals. Section 4 delineates the fundamental components of signal design for LIB impedance measurement. Section 5 examines the utilization of perturbation signals in onboard battery management systems. Sections 6 and 7 delineate the principal conclusions and prospects.

## 2. Battery Impedance Spectrum

The impedance of the battery typically characterizes its dynamic response to a disturbance signal at a specific frequency, serving as a crucial metric for assessing lithium battery performance. The fundamental principle involves applying a low-amplitude sinusoidal current excitation signal to the lithium battery. By examining the correlation between the frequency and amplitude of the excitation signal and the resultant response signal, the

frequency response of the system under investigation within a specified frequency range is ultimately derived.

The construction of the battery impedance spectrum requires the acquisition of impedance responses across various frequencies. The impedance spectrum of a standard lithium-ion battery, as depicted in Figure 1, consists of four unique segments, each of which has specific relevance [13]. The ultra-high-frequency segment (above 1000 Hz) is represented by the inductive impedance, which corresponds to the battery's ohmic resistance $R_{Ohm}$ and inductance L; the high-frequency segment (about 100–1000 Hz) of the curve appears as a semicircle, corresponding to the lithium-ion impedance through the solid electrolyte (including the solid electrolyte interface film, etc.). $R_1$ and $C_1$ denote the resistance and capacitance of the solid electrolyte interface membrane; the semicircle in the mid-frequency region (around 1–100 Hz) signifies the charge transfer impedance, also referred to as the electrode polarization impedance, while $R_2$ and $C_2$ indicate the charge transfer resistance and double-layer capacitance, respectively; the 45° straight line in the low-frequency region (around 0–1 Hz) represents the Li-ion diffusion impedance, commonly known as the concentration polarization impedance or Warburg impedance [14,15]. Note that the frequency segments vary depending on battery configuration and chemistry.
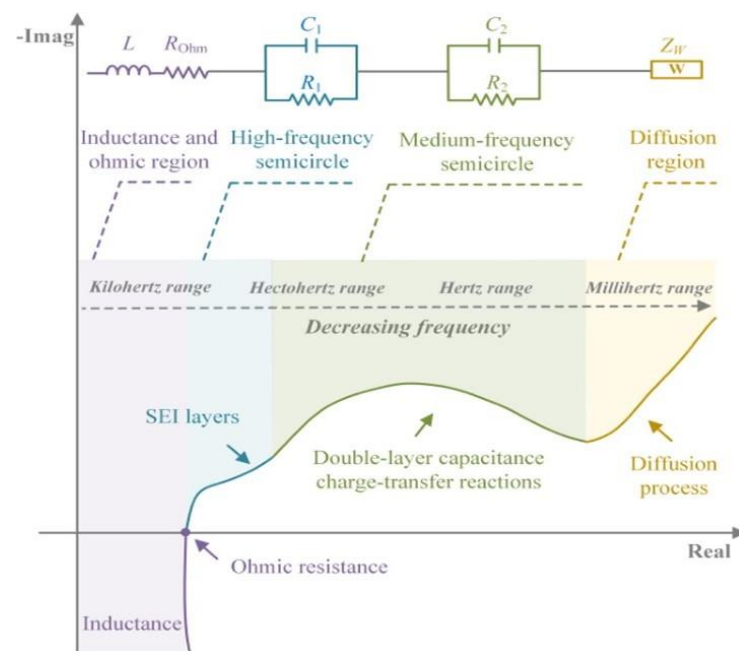


**Figure 1.** Nyquist diagram representing the impedance spectrum of the battery in equivalent circuit model components [16].

### 2.1. Inductive and Resistive Area

The impedance of the ultra-high frequency portion comprises the ohmic resistance $R_{Ohm}$ and the inductance L, which exists at frequencies exceeding thousands of hertz. The inductive component is affected by the inductance of the collector wire and the inductance of the test coils, while the resistive component comprises the electrolyte, electrodes, diaphragm, and electrical contact resistance of the cell [17]. The conductivity of the electrolyte is a primary element influencing the resistance of this component; higher conductivity enhances ion migration, hence impacting resistance [18]. The impedance in this frequency range is influenced by both temperature and battery health state. The ohmic impedance increases more rapidly at higher temperatures than at room temperature [19]. As the battery degrades, the ohmic resistance changes due to the loss of the electrolyte and the graphite anode [20].

## 2.2. Solid Electrolyte Interface Layers Area

The EIS plot in the high-frequency range demonstrates the inductive impedance characteristics related to solid electrolyte interface (SEI) layers, with characteristic frequencies ranging from kilohertz to hundreds of hertz. In electrocatalytic processes, the catalytic influence of reaction intermediates adsorbed on the electrode surface diminishes reaction impedance, resulting in a high-frequency semicircle linked to sensing impedance within the kilohertz to hundred-hertz range of the impedance spectrum [21]. The configuration of the semicircle in the high-frequency impedance spectrum correlates with the decomposition of the electrolyte and the growth of the SEI film [22]. The formation of the SEI film is profoundly affected by the electrode material, electrolyte, and solvent of the battery, leading to the depletion of lithium ions in the electrolyte, which causes lithium metal precipitation and results in an irreversible capacity loss of the battery [23]. The creation of a dense SEI film ideally prevents direct contact between the electrolyte and the electrode surface, mitigating battery leakage and protecting the graphite structure; nevertheless, the SEI film may also result in increased impedance.

## 2.3. Charge Transfer Kinetics Area

The mid-frequency impedance typically manifests around hundreds of Hertz, positioned between the semicircle linked to the diffusive migration of lithium ions through the SEI layers on the electrode's active material surface and the semicircle related to charge transfer kinetics. Furthermore, the semicircle in the mid-frequency domain exhibits a larger magnitude on the impedance spectrum compared to the semicircle in the high-frequency domain [24]. This impedance semicircle is presented by the charge transfer internal resistance $R_{CT}$ and the double layer capacitance $C_{dl}$ in parallel, as expressed in the following equation:

$$R_{CT} = \frac{RT}{nFJ_0},\tag{1}$$

where $R$ is the air constant, $T$ is the absolute temperature, $n$ is the amount of substance of the electrons participating in the reaction, $F$ is the Faraday constant, and $J_0$ is the exchange current density.

$$C_{dl} = 1/(2\pi f_{max} R_{CT}),\tag{2}$$

where $f_{max}$ is the frequency corresponding to the local maximum value of the imaginary part of the semicircle.

The impedance of charge transfer kinetics is related to the temperature and current, as the characteristics of charge transfer resistance are contingent upon the electron mobility. The double-layer capacitance is defined by two layers of oppositely charged particles formed at the interface between the electrode surface and the electrolyte [25].

## 2.4. Diffuse Processes Area

The low-frequency component in Figure 1 is predominantly influenced by the cell's diffusion process of $Li^+$ in the LIB electrolyte, represented by the Warburg impedance $Z_W$ [26]. The EIS Nyquist plot displays a straight line at about 45° to the X-axis, influenced by the state of charge, excitation current amplitude, battery capacity, and the number of charge/discharge cycles [27]. The diffusion coefficient of lithium ions within the electrolyte is the principal kinetic parameter of the diffusion process and indicates the electrode's capacity for high-rate discharges, computed as follows:

$$Z_W = \frac{W}{(j\omega)^{\frac{1}{2}}},\tag{3}$$

where $\omega$ denotes the angular frequency, and $W$ is the Warbug coefficient.

## 3. Classification of Perturbation Signals

Section 2 illustrates that the battery impedance is frequently employed to characterize the LIB dynamic response when exposed to excitation signals at particular frequencies. Nonetheless, the widely utilized EIS technique is time-intensive, necessitating many hours for testing within a particular frequency band. In recent years, researchers have garnered significant interest in broadband perturbation signals in rapid battery characterization [28]. The perturbation excitation signals are chiefly classified as sine-sweep signals, step signals, square-wave signals, pseudo-random sequences, and multisine signals. This section introduces novel perturbation signals, examines their limitations, and delineates the potential enhancement strategies.

### 3.1. Sine-Sweep Signal

A sine-swept signal is a sinusoidal waveform with a frequency that fluctuates logarithmically with time, either increasing or decreasing sequentially. The sine-swept signal, fundamental to the EIS technique, measures a battery's impedance at different frequencies by injecting sinusoidal currents or voltages, acquiring the battery's frequency response, and subsequently computing the resultant impedance spectrum for analysis.

Dam et al. employed a sinusoidal sweeping signal injected into a battery to conduct a frequency analysis of the impedance spectrum within the range of 100 mHz to 100 Hz, with a total measurement duration of 97 s [29]. Wei et al. employed a sinusoidal sweeping signal to assess and analyze the impedance spectrum of a battery within a frequency range of 0.1 Hz to 500 Hz [30]. To mitigate the prolonged measurement duration of the sinusoidal sweep signal and the significant stability issues encountered when measuring low frequencies below 1 Hz, Kallel et al. introduced an innovative design for sinusoidal excitation signals [31]. This design establishes a virtual interval to optimize the spacing between the crest factor and frequency samples, enhances the stability of the measurement system, decreases measurement time, and employs a Kramers–Kronig-based approach. The stability was evaluated utilizing the linear Kramers–Kronig (LKK) method, revealing that across the frequency spectrum of 10 mHz to 1 kHz, the root mean square error of the LKK diminished by 84% relative to the sinusoidal sweep signal, while the measurement duration decreased from 1440 s to 315 s.

The sine-sweep signal offers advantages such as power concentration, high precision, and ease of frequency modification during measurement. The measurement duration is excessively prolonged, particularly for low-frequency impedance, and the intricate signal design necessitates complex hardware, rendering it prohibitively expensive for non-laboratory applications. Additionally, the lengthy injection time into a cell complicates the feasibility of onboard measurement.

### 3.2. Step Signal

To enhance the precision of impedance acquisition and streamline the measurement process, the researchers employed a step signal as a perturbation, which improves the signal-to-noise ratio and encompasses additional harmonic components [16]. The step signal is easier to generate than the sinusoidal sweep signal and may be produced using a standard charging and discharging mechanism, hence enhancing the simplicity and feasibility of quick impedance measurements. The step signal waveform possesses a broader spectrum of harmonics and can accurately represent impedance values across many frequencies [32].

Gabrielli et al. examined the application of white noise and step signals in measurement techniques, emphasizing practical implementations [33]. Su et al. introduced a step signal utilizing Gaussian process regression, wherein a step perturbation signal was introduced into the battery during charging via the collaboration of a battery management system and a bi-directional converter, resulting in the extraction of six Li-ion battery health metrics and achieving a specific frequency range [34]. The impedance tests span the frequency range of 10 mHz to 2 Hz, with the step signal response at each frequency

being analogous to that of the sinusoidal signal at the corresponding frequency. Hoshi et al. and Itagaki et al. conducted Morlet wavelet transforms on step current signals and their corresponding voltage responses to calculate impedance throughout the frequency range of 0.1 Hz to 100 Hz [35,36]. The battery temperature is determined by the battery impedance at a designated frequency during dynamic operation conditions. Wang et al. initially introduced a rapid computation method for broadband battery impedance utilizing the S-transform, which employs a Gaussian window of specified width and frequency to address step perturbation signals and the battery response, significantly diminishing the requirements for broadband impedance acquisition [37]. Simultaneously, the perturbation signal and battery response can be produced using standard charging and discharging apparatus, and this method reduces acquisition time by at least 19% compared to the sinusoidal swept signal while decreasing computation time by at least 84% relative to the previously proposed wavelet transform.

Despite the step signal's straightforward composition and elevated signal-to-noise ratio, facilitating impedance measurement, it possesses an inhomogeneous power spectrum, with the majority of its power concentrated in the fundamental harmonics, potentially leading to measurement inaccuracies in impedance.

### 3.3. Square Wave Signal

A square wave signal is a prevalent non-sinusoidal waveform and a standard analogue circuit signal characterized by constant amplitude, adjustable duty cycle, adjustable phase, and excellent stability. It finds extensive applications in switching power supplies, audio signals, digital circuits, and sensor signals. Additionally, it shares similarities with step signals, exhibiting reduced amplitude and a higher harmonic content.

Yokoshima et al. employed square waves for impedance measurements in a simple redox reaction of $[Fe(CN)_6]^{4-}/[Fe(CN)_6]^{3-}$ solution and lithium-ion batteries [38]. It achieves stable impedance responses within the frequency ranges of 40 Hz to 3.5 kHz for the former and 5 Hz to 2.5 kHz for the latter, with measurement errors between these methods and conventional EIS being less than 3%. In addition, these authors posited that the precision of impedance measurements is contingent upon the signal-to-noise ratio of the harmonic power spectrum and the attenuation rate of the Fourier series impedance measurements [39]. The accuracy was enhanced by modifying the input waveforms to approximate the ideal Fourier series waveforms, in conjunction with employing a simple moving average filter and an overall average. Wang et al. determined that the essential factor in measuring battery impedance is the integration of the power conversion circuit within the EIS detection system [40]. They demonstrated that a large square wave excitation signal can be decomposed into a direct current (DC) component and several diminishing odd harmonic components, each amenable to analysis akin to that of a sinusoidal waveform. Consequently, a square wave excitation device with a microsecond response speed was developed, employing a method for current control and voltage limitation to facilitate safe, reliable, and rapid measurements.

Despite the benefits of constant amplitude, robust stability, and straightforward modulation of the square wave signal, unstable output voltage arises when the duty cycle of the injected square wave signal is substantial [41]. Furthermore, the precision of the cell response is constrained by the signal-to-noise ratio of the power spectrum and the power controller generating the signal [39]. Additionally, the power controller produces a degraded square wave when the measurement duration is reduced, adversely impacting measurement accuracy. Consequently, the optimization of the square wave signal necessitates additional investigation.

### 3.4. Pseudo-Random Sequence Signal

The sinusoidal scanning signal represents a concentrated power station at a singular fundamental frequency to enhance the signal-to-noise ratio and optimize measurement accuracy. However, this method is time-consuming, particularly at low frequencies, and

the sinusoidal signal exhibits multiple amplitudes simultaneously, further complicating the injection process. The pseudo-random sequence (PRS) signal exhibits characteristics of straightforward signal composition, diverse frequency components, a more uniform power spectrum, and multi-frequency superposability relative to the aforementioned signals [42]. Furthermore, in comparison to sinusoidal scanning signals, the pseudo-random sequence introduced in the article [43] reduces time expenditure by 73%, thereby establishing the superiority of the pseudo-random sequence. Consequently, pseudo-random sequence signals are increasingly utilized in the acquisition of battery impedance.

The maximum length sequence (MLS) represents the fundamental category within the PRS family and can be easily produced utilizing a linear feedback shift register [44]. The parameter length $N$ in the MLS is defined by the subsequent equation:

$$N = 2^n - 1. \tag{4}$$

Here, $n = 1, 2, 3, \ldots$ denotes the order of the shift registers. In contrast to the square wave and step perturbation signals, the PRS signal has a near-band-limited white noise characteristic in frequency, with a power spectrum that displays a nearly uniform distribution.

The power content of the PRS signal is expressed using the following formula:

$$P(k) = I_m^2 \frac{2(N+1)}{N^2} \left( \frac{sin\pi k/N}{\pi k/N} \right)^2, \tag{5}$$

where $P(k)$ denotes the power of the $k$th harmonic, and $I_m$ and $N$ denote the amplitude and length of the PRS signal.

The aforementioned equations indicate that as the sequence length $N$ increases, the signal power significantly decreases, leading to an inadequate signal-to-noise ratio between the altered signal and the response output, hence adversely impacting measurement accuracy. Sihvo et al. proposed employing a ternary sequence signal as the perturbation signal to enhance the signal-to-noise ratio and utilized a moving average filter (MAF) to correct the impedance bias at high frequencies [45]. However, the efficacy of the MAF diminishes when measurements exhibit significant value discrepancies and a low-frequency region with substantial bias persists. Liebhart et al. introduced a weighted overlapping segment averaging technique to refine impedance measurements; however, the parameter configuration necessitates specialized debugging and is impractical for real-world applications [46]. To enhance the signal-to-noise ratio for mitigating interference with impedance measurements, Du et al. developed a series of double PRS signals utilizing two distinct sub-sequences that measure varying frequency ranges of battery impedance [43]. This approach reduces the length of the PRS signal while enhancing its power content, offering advantages such as high efficiency, low computational cost, and ease of implementation, thereby providing researchers with a novel perspective on signal processing.

Despite the signal's benefits of reduced measurement and injection durations, along with the capability for multi-frequency superposition, its deficiency in harmonic power content renders it susceptible to noise interference, thereby diminishing the precision of impedance measurements. Furthermore, the conflict between the measurable bandwidth and the signal-to-noise ratio of the PRS signal employed for battery impedance measurement should be addressed to address substantial impedance bias in both low-frequency and high-frequency domains, thereby achieving reliable broadband impedance measurements.

### 3.5. Multisine Signal

The fast measurement of battery impedance by multisine signals has garnered significant interest and is extensively employed. The multisine signal, created by superimposing multiple frequency sinusoidal signals, has been utilized for impedance spectra and transfer function studies across various domains, including biomedical applications, material characterization, and battery impedance measurement [43].

Macdonald et al. examined multisine s measurements of nickel–metal hydride (Ni-MH) batteries, along with half-cell assessments of lithium-ion cathode and anode materials at various discharge levels [26]. Schmidt et al. employed a multisine-based impedance spectroscopy method to acquire the impedance spectrum of the battery within the frequency range of 0.1 Hz to 1000 Hz during discharge, validating the impedance model of the lithium-ion battery cell [47]. Widanage et al. devised a pulse-multisine signal to measure impedance in the low-frequency spectrum [48]. The subsequent equation illustrates the general throughput of the multisine signal:

$$u(t) = \sum_{n=1}^{N} A_n cos(2\pi f_n t + \varphi_n), \tag{6}$$

where $t$ is the time, $N$ is the number of excitation frequencies, $f_n$ is the $n$th excitation frequency, $A_n$ is the amplitude, and $\varphi_n$ is the phase of $f_n$, $n = 1, ..., N$. The aforementioned equation indicates that the parameters in multisine signals are not predetermined, thereby providing greater flexibility in designing the signal's frequency components to generate an arbitrary spectrum, making it particularly suitable for fast Fourier transform estimation of broadband excitation signals [49].

Nevertheless, the intricate signal harmonics and substantial peak-to-peak variation of the multisine might induce non-linearities in the cell, compromising the precision of the frequency response. To address the aforementioned issue, the crest factor of the signal can be diminished by altering the phase $\varphi_n$ to mitigate the impact. Yang et al. utilized a clipping strategy that combines repeated signal clipping with the reapplication of the clipped signal phase of the multisine to reduce the crest factor [49]. Kallel et al. proposed a novel signal design methodology to reduce the crest factor by allocating frequency components within a virtual interval framework, thus significantly shortening scan time while maintaining stability in the low-frequency range [31]. Janeiro et al. and Horner et al. proposed the utilization of artificial bee colonies and genetic algorithms to enhance the crest factor of the multisine signals, respectively [50,51].

In recent years, investigations on the characterization of the non-linear behavior of batteries have intensified. Firouz et al. employed multisine signals with various random phases to analyze battery dynamics, which identify the linear components of the battery, non-linear distortions, and noise disturbances [52]. Fan et al. utilized a random phase odd multisine signal in an experimental three-electrode NMC/silicon graphite battery to examine the battery's non-linearity inside a positive and negative system [53]. A rapid frequency domain method was employed to ascertain the frequency response function of the system, revealing that the primary source of non-linearity is the cathode. The multisine-based non-linear method also elucidated the reasons for the low state of charge accuracy in linear equivalent circuit models [54]. Subsequently, the correlation between the non-linearity of the lithium-ion battery system and battery aging was established using a sinusoidal-based non-linear characterization technique [55].

The multisine-based methods for assessing battery impedance not only decrease the measurement length but also preserve battery stability during the process, thereby attaining a very precise assessment. The parameters, including duration, frequency distribution, and power density of the multisine signal, can be modified flexibility to offer considerable flexibility in signal design. Additionally, the non-linear characterization method utilizing this signal exhibits reduced operational time, facilitating the analysis of the non-linear behavior of electrochemical reactions, thereby allowing for further exploration of the signal's potential. In conclusion, the multisine-based methods effectively capture both impedance and non-linear information, facilitating enhanced implementation in BMS to optimize battery utilization and inform future battery design.

*3.6. Comparison of Signals*

Table 1 lists the aforementioned perturbation signals employed for impedance measurements and the comparison of signal features. The sine-swept signals exhibit excep-

tionally high signal-to-noise ratios (SNR) and precise frequency response accuracy [30]. The method offers advantages, including the capacity to focus power at a singular frequency, yet the necessary measurement duration remains excessively prolonged, particularly for extremely low-frequency impedance. The requirement for complex hardware design in its signal injection makes it rarely utilized in real applications. Step signals have a wider harmonic spectrum and can effectively represent impedance values across different frequencies [32]. However, they display an uneven power spectrum, with most power concentrated in the fundamental harmonics, limiting their effectiveness in measuring impedance at multiple frequencies [42]. Square wave signals provide benefits like limited amplitude and improved stability. Nonetheless, these signals are inherently limited by the duty cycle and the signal-to-noise ratio of the power spectrum, which may lead to complications with degraded square waves [39]. Pseudo-random sequence signals exhibit finite amplitude, varied harmonics, and a consistent power spectrum, rendering them appropriate for impedance measurements across all frequency ranges [42]. Nonetheless, their signal-to-noise ratio is inadequate, requiring additional processing for impedance measurements. The properties of multisine signals, such as duration, dispersion, and frequency density, can be adjusted flexibly, providing significant design freedom. Nonetheless, this complexity and heightened peaking factor undermines the accuracy of impedance measurement [31].

**Table 1.** A comparison of features between different perturbation signals.

| Perturbation Signal | Schematic Representation | Advantages | Constraints |
|---|---|---|---|
| Sine-sweep | | Maximized SNR and excellent frequency response accuracy | Intricate signal injection process and time-consuming |
| Step | | Finite amplitude levels and simple implementation process | Uneven power spectrum and limited measurable bandwidth |
| Square wave | | Abundant frequency components and simple implementation process | Requirements on signal generator and low measurement accuracy |
| PRS | | Abundant frequency components and simple implementation process | Numerous amplitude levels and large peak factor |
| Multisine | | Flexible design of frequency components and rapid signal injection | Inadequate SNR and requirements on impedance filtering |

## 4. Elements of the Signal Design

It is essential to emphasize that, in the majority of impedance applications, the accuracy of the measured impedance spectrum is of paramount significance [10]. The precision of the measured impedance spectrum is intricately linked to the signal design. The benefits of perturbation signals include flexibility of parameter configurations, such as signal amplitude, signal-to-noise ratio, and power spectrum, during the signal design procedure. This section will examine the factors affecting the signal and the rationale for the precision of the impedance spectrum measurement.

### 4.1. Signal Amplitude

In battery impedance spectroscopy, the excitation signal must remain within the linear range of the current-voltage characteristic. Conversely, the Parseval theorem states that the amplitude levels in the time domain correspond to the amplitude levels in the frequency domain [56]. The amplitude of the signal affects the crest factor, which denotes

the ratio between the effective value of a signal and its peak, rendering it essential for attaining optimal signal strength throughout all excitation frequencies. Consequently, in the impedance spectrum, the excitation signal's amplitude must be constrained to ensure linearity, and its duration must be restricted to maintain stability [57].

For instance, excessively large crest factors of multisine signals may induce non-linearity of a LIB, leading to worse accuracy in impedance spectrum measurements. The signal's amplitude predominantly influences measurements in the low and medium frequency ranges of the impedance response, where excessively high crest factors may induce significant non-linearities. The impedance value in the high-frequency region is primarily influenced by the characteristics of the cell itself, together with additional parameters such as the SEI layers and the electrolyte within the cell [58]. The impedance results of the complete cell at various AC amplitudes and temperatures are presented in Figure 2.
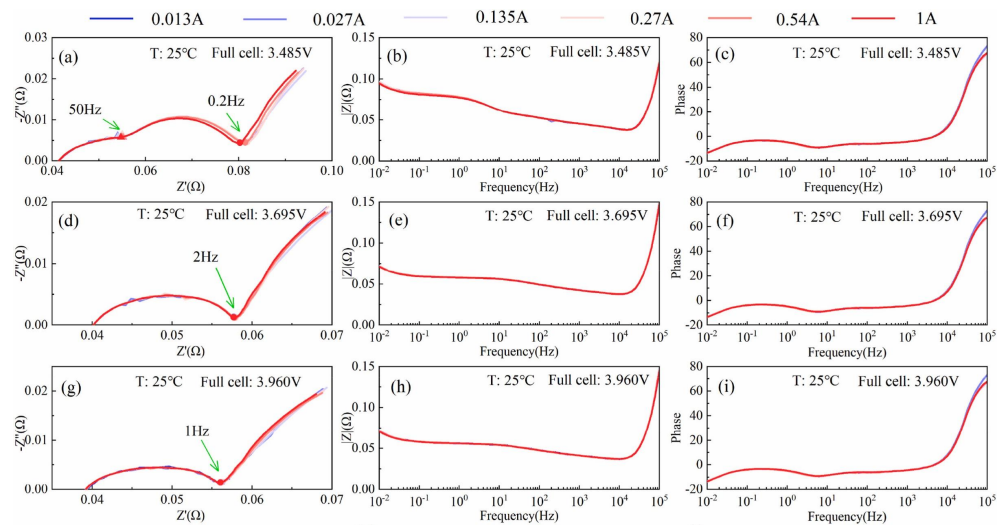


**Figure 2.** (**a**–**i**) The impedance response of the full cell with different AC amplitudes (0.013 A, 0.027 A, 0.135 A, 0.27 A, 0.54 A, 1 A) at 25 °C [59].

Figure 2 illustrates a slight decrease of impedance at low SOC levels, exclusively within the medium and low-frequency bands at 25 °C. No significant change is observed in the impedance arcs of medium and high SOC levels as the alternating current (AC) amplitude increases. The impedance in the mid and low-frequency regions for impedance arcs of low SOC levels are slightly influenced by AC amplitude, with the fluctuation being insignificant. Moreover, no substantial difference is apparent in the Bode plots at 25 °C for Figure 2. At −10 °C, the impedance at medium and low-frequency ranges is significantly affected by changes in AC amplitudes, regardless of the SOC levels [59].

### 4.2. Signal-to-Noise Ratio

During the measurement of battery impedance, the excitation and response signals, along with any noise disturbances, are acquired concurrently. The measured impedance is denoted as $Z_1$, while the real impedance is denoted as $Z_2$. The equation is as follows:

$$Z_1(f_k) = \frac{V_a(f_k) + V_n(f_k)}{I_a(f_k) + I_n(f_k)}, \tag{7}$$

$$Z_2(f_k) = \frac{V_a(f_k)}{I_a(f_k)}, \tag{8}$$

where $V_a$ and $V_n$ represent the actual and noisy voltage signals, and $I_a$ and $I_N$ correspond to the current signals. The error between the two impedances is denoted as $|\triangle Z(f_k)|$, which can be calculated as follows:

$$|\triangle Z(f_k)| = \left| \frac{SNR\frac{e^{j\triangle\varphi_v}}{v,f_k} - SNR\frac{e^{j\triangle\varphi_i}}{i,f_k}}{\left(SNR\frac{e^{j\triangle\varphi_v}}{v,f_k}\right)\left(SNR\frac{e^{j\triangle\varphi_i}}{i,f_k} - 1\right)} \right|,$$

(9)

where $\triangle\varphi_i$ denotes the divergence in phase between $I_a$ and $I_n$. $\triangle\varphi_i$ denotes the phase divergence between $I_a$ and $I_n$. $SNR_{v,f_k}$ and $SNR_{i,f_k}$ denote the SNRs of the measured voltage and current signals.

The aforementioned equation illustrates that the amplitude, phase, and frequency of the signal can influence the signal-to-noise ratio. The objective of minimizing the mistake can be accomplished by decreasing the signal's amplitude or modifying the signal's frequency component [60].

*4.3. Power Spectrum*

The power spectrum defines the distribution of a signal's power across varying frequencies. An inhomogeneous power spectrum may restrict the accuracy of the signal used to assess cell impedance response across various frequency ranges [61]. For any signal $x(t)$, let

$$x_T(t) = x(t)rect\left(\frac{t}{T}\right)$$

(10)

denote a "time-windowed" projection of $x(t)$ taking value zero outside of the interval $[-T/2, T/2])$, where $T > 0$. Assume, for each $T$, that the Fourier transform of $x_T(t)$ exists and is given by $x_T(f)$.

Since white noise is a stationary process, according to the Wiener–Khinchin theorem, as follows:

$$S_x(f) = \lim_{T\to\infty} \frac{1}{T}|X_T(f)|^2$$

(11)

where $S_x(f)$ quantifies the contribution to the power of $x$ from complex-exponential signal components at frequency $f$. The overall power corresponding to $x$ is subsequently expressed as

$$P_x = \int_\infty^{-\infty} S_x(f)df.$$

(12)

In summary, the perturbed signal will possess a matching power at each frequency, enabling the power spectrum to be integrated with the cell impedance. When the power spectrum value is diminished, the signal becomes less informative and is less likely to represent a legitimate value [62]. Meng et al. introduced a fusion algorithm that integrates the power and frequency attributes of impedance measurements, leveraging the inherent relationships among impedance, frequency, and power spectra to establish an innovative fusion mechanism, resulting in the efficient extraction of battery impedance via an automated selection process [42]. Consequently, the power spectrum serves as a crucial statistic for assessing signals across various frequencies.

## 5. Applications of Battery Impedance

Battery impedance has been extensively utilized for the development of essential functions in battery characterization and performance analysis. The perturbation signals, designed to facilitate the rapid acquisition of battery impedance, are intended to be developed as onboard impedance characterization methods. This section reviews essential operations such as battery health prediction, charge state estimation, battery defect diagnostics, parameter estimation, and battery modeling, emphasizing the importance of developing characterization methods of perturbation signals.

The batteries currently discussed in this section are mainly experimental batteries and commercial batteries. The batteries used in the experiments can be either commercial batteries or experimental batteries. Experimental batteries for research on lithium batteries mainly include three-electrode experimental batteries and button batteries. Commercial

batteries mainly refer to cylindrical batteries, square batteries, and soft pack batteries. Cylindrical batteries have high stability, standard size, reliable thermal management and high power density, but the packaging efficiency of the battery module is low; square batteries have a slightly lower energy density, but the design is robust; pouch batteries are lightweight and flexible, and the power density can be changed according to the design, but the stability is poor, and is prone to expansion. Cylindrical and soft-packed batteries are used to improve the repeatability of EIS measurements [63] or to study electrodes during cycling [64]; button batteries are commonly used to study the electrochemical properties of component materials [65]; three-electrode batteries are able to decouple the potentials of the positive and negative electrodes, focusing more on the electrode dynamics but are difficult to be applied in practice because they need to be disassembled and fabricated [53]. The experimental cell is exemplified by a three-electrode cell. The electrode structure of a three-electrode cell consists of a cathode, an anode, and a reference electrode (RE). The RE should exhibit reversible, ideally unpolarized, stable, and reproducible potentials under all conditions experienced during electrochemical measurements [66]. In situ monitoring of individual electrode potentials allows for the analysis of the different operational effects on each electrode [67]. Thus, the three-electrode cell is capable of monitoring the lithium-ion battery's lithium-dissolution behavior under different conditions. RE is very sensitive to experimental conditions such as electrolyte selection and design and is not as safe as commercial batteries [68]. EIS measurements using RE can isolate the various contributions from individual battery components (i.e., diaphragm, electrolyte, collector, and electrodes), which can aid in experimental investigations of EIS [69]. In conclusion, commercial and experimental batteries have their own advantages and disadvantages. When researching EIS, each battery has its own emphasis on applicability, and the choice needs to be based on practical decisions.

### 5.1. Battery Health Prediction

The state of health of a lithium-ion battery is a critical metric that indicates the extent of the battery's aging, denoted by the ratio of residual capacity to original capacity, with 100% indicating a new battery and 80% signifying a retired battery. With an increase in the number of cycles, the maximum accessible capacity diminishes as the internal resistance escalates. A BMS must be capable of evaluating the battery SOH, issuing danger alerts, and maintaining safe and stable battery functionality over time. The identification of battery degradation mechanisms analysis is also crucial for a novel BMS, as illustrated in Figure 3, which depicts the aging mechanisms of Li-ion batteries, including the creation and expansion of the SEI layer, as well as electrode and electrolyte degradation, among other variables [6]. An understanding of degradation mechanisms is essential for predicting battery health [7]. Moreover, precise SOH estimation can enhance battery economics and facilitate the optimization of charging and discharging procedures, hence preventing battery overuse.
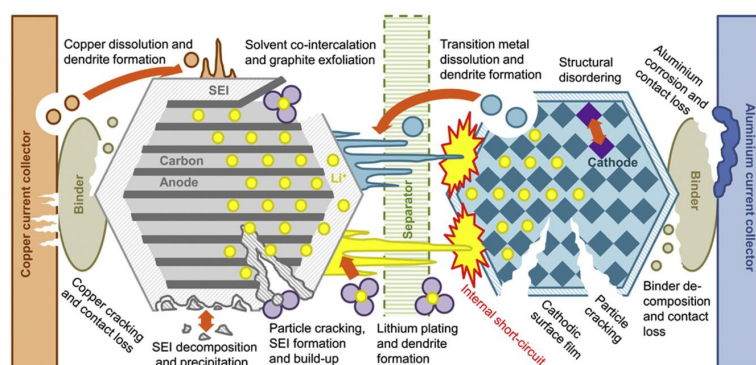


**Figure 3.** The most common lithium-ion battery degradation mechanisms in lithium-ion batteries [6].

The degradation of Li-ion batteries is attributed to alterations in the battery electrode interface [70]. Factors such as the formation of the solid electrolyte interphase film, depletion of active lithium materials and electrolytes, and loss of active materials in both cathode and anode are primary contributors to capacity decline [71]. The benefits of electrochemical impedance spectroscopy, which can elucidate the kinetics of the battery's reactive processes and the structural characteristics of the electrode interface, offer theoretical support for SOH estimation based on electrochemical impedance spectra.

The aging degradation mostly increases ohmic resistance for the evaluated Li-ion battery while exerting no substantial effect on charge transfer and diffusion processes [72]. Sun et al. present a novel approach for obtaining the impedance spectrum via a convolutional neural network, as illustrated in Figure 4, which employs impedance measurements at various characteristic frequencies as input [73]. The algorithm's input consists of impedance measurements taken at various characteristic frequencies within the mid and high-frequency ranges. The suggested method can reliably get the impedance spectrum and rapidly adjust to various battery states and chemistry by integrating straightforward measurements with model-based predictions. The experimental results confirmed that the predictions aligned with the actual values, with a maximum root mean square error of 0.93 m$\Omega$. Liu et al. claimed that most aging processes in Li-ion batteries have no correlation solely with a specific region on the impedance curve and that the same region may be affected by multiple aging mechanisms [12].
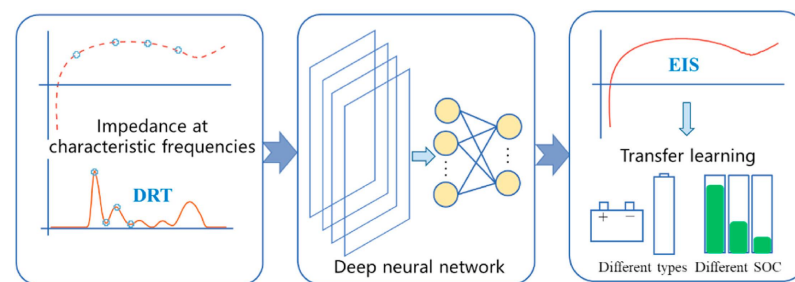


**Figure 4.** Process for obtaining impedance spectra using impedance features as input to a convolutional neural network [73].

In Section 2, the Nyquist plot of the impedance spectrum of the Li-ion battery was categorized into four distinct regions: the inductive and resistive area, the SEI layer area, the charge transfer kinetics area, and the diffusion processes area. The influence of the battery's SOH on these four impedance regions will be examined subsequently. The dimensions of the inductive and resistive area are primarily dictated by the resistance of the electrolyte while also being influenced by the resistance among the electrode metal, electrode leads, terminals, and contacts. Furthermore, the resistance value of the impedance and inductance region markedly escalates with the depletion of lithium ions in the electrolyte. Figure 5 illustrates the correlation between Li-ion batteries and aging in electric vehicles [74]. The ohmic resistance of the batteries at three temperatures progressively increased with the distance traveled, suggesting that the impedance value in this context can serve as an indicator of battery aging. Yoshida et al. measured the thickness of the SEI film and determined that the increase in resistance within the ohmic zone correlated with the growth of the SEI layer [75]. Schindler et al. ascribed the rise in ohmic resistance to the corrosion of the current collector and the decomposition of the electrolyte, alongside the SEI film's growth, which further influenced the impedance value in the high-frequency region [76].

The impedance in the high-frequency range is influenced by the development of the SEI film as the graphite electrode ages within the cell [77]. This reaction generates a lithium-containing SEI layer on the electrode surface, which obstructs the electrolyte's access to the electrode and impedes lithium insertion. Consequently, the proliferation of the SEI results in a depletion of recoverable lithium, thereby diminishing the battery's capacity [73]. Witt et al. provide a solution that integrates physicochemical SEI and cell

modeling for the concurrent analysis of both measurement types [78]. The interfacial and bulk characteristics of the SEI were examined, emphasizing the significance of SEI thickness and ionic conductivity on cell performance. Figure 6a illustrates the analysis of the impact of SEI thickness on the impedance response. It is evident that it predominantly produces a higher impedance at the $Z_{0-axis}$ intercept at elevated frequencies, accompanied by a parallel shift of the entire spectrum. This pertains to its influence on the ohmic resistance of the surface coating and, consequently, the total ohmic resistance of the cell. Figure 6b illustrates the impact of the SEI ionic conductivity. A reduced conductivity mostly influences the Z0-axis intercept at elevated frequencies without a corresponding increase in low-frequency impedance. Its conductivity impacts the potentials in both the active material and the electrolyte phase.
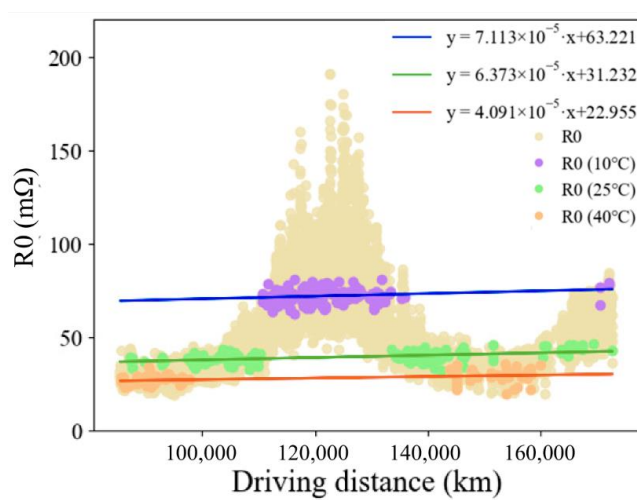


**Figure 5.** Describing the relationship between the ohmic resistance of lithium batteries in electric vehicles and the driving distance by electric vehicles using linear regression at different temperatures [74].

The development of machine learning algorithms has also made great strides in current research. Advances in algorithms have improved the accuracy of EIS calculations, overcoming the trade-off between accuracy and efficiency for researchers. Many researchers use EIS features as machine learning inputs to predict battery health. Bao et al. [79] compared six machine learning models of varying complexity to reveal the accuracy and reliability of battery health prediction. Bao et al. extracted the statistical features of the EIS data using the mean and extreme values of the impedance. Twenty features were extracted from 120 data points in each cycle to effectively retain trends in the high and low-frequency portions of the data. Six machine learning models with different levels of complexity were used to reveal the accuracy and reliability of battery health prediction. The results indicated that the MLP model had a mean absolute error (MAE) of 0.17, a mean square error of 0.32, a root mean square error of 0.40, and a mean absolute percentage error of 0.97 %. After combining these features, the MAE of the XGBoost model was 0.05. Wang et al. [80] chose the point at 10 kHz, the leftmost point of the curve, and the vertex on the charge-transfer impedance segment, as shown in Figure 7, as feature points of EIS as inputs to four machine learning models (CatBoost, random forest, support vector machine, and deep neural networks), the relationship between aging features and EIS was explored. The results show that the accuracy of the EIS features in classifying that the battery resistance can reach 100% under certain conditions. It is also found that the features extracted from EIS curves are more suitable for applications with high power requirements. In addition to the possibility of choosing EIS curve features as inputs to machine learning, there are also many researchers who use physical features [81] and data [82,83] from batteries as inputs.
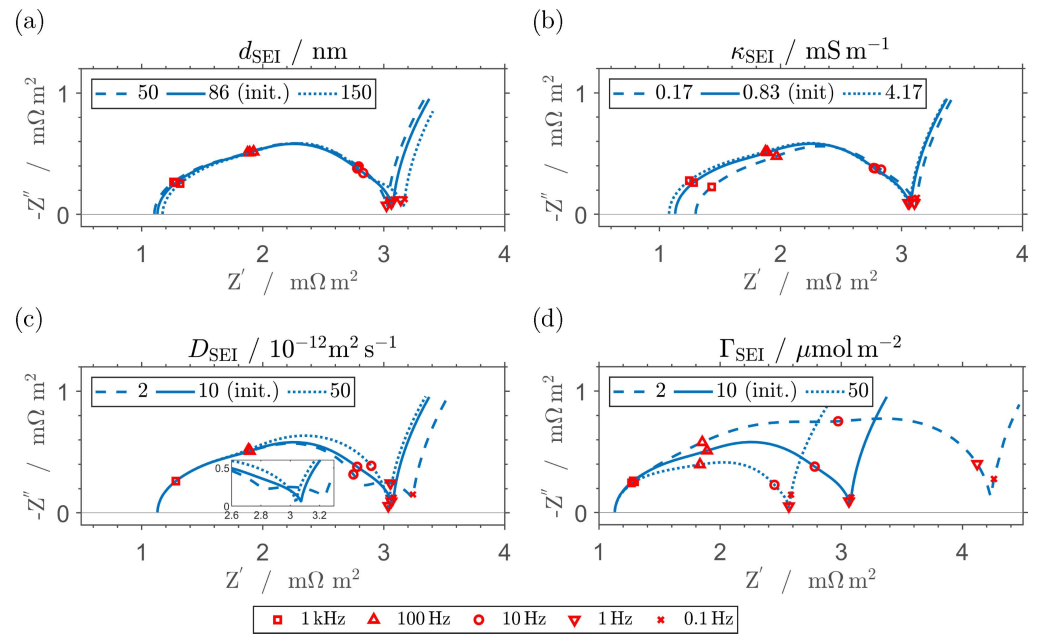
**Figure 6.** Simulated full-cell impedance spectra at 3.7V with the parameterized model for a variation of (**a**) SEI thickness, (**b**) ionic conductivity of the SEI, (**c**) diffusion coefficient of lithium in the SEI, and (**d**) SEI surface site density (five frequencies are highlighted in red: 1 kHz, 100 Hz, 10 Hz, 1 Hz, and 0.1 Hz) [78].
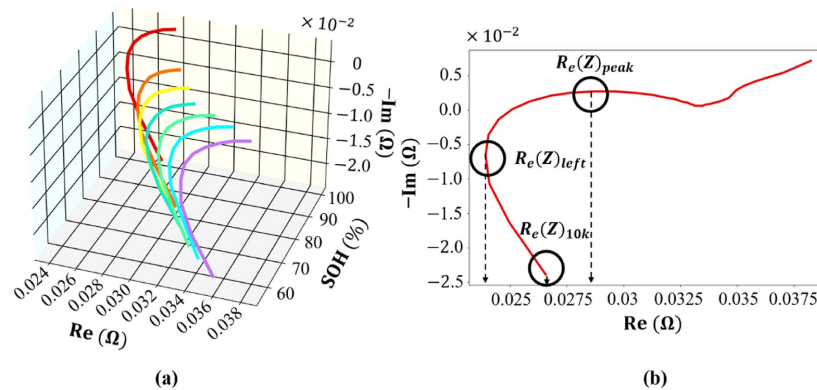


**Figure 7.** EIS curves of one NMC battery at 25 °C. (**a**) Variation of the Nyquist plots under different SOHs, where the low frequency range is not taken into account. (**b**) Three features selected from the EIS curve. [80].

The magnitude of the impedance value in the mid-frequency region is determined by the depletion of the cathode active material, including the double-layer capacitance and charge transfer resistance present at the interface between the battery electrodes and the electrolyte, which produces a double-layer effect at the interface when ions are adsorbed onto the surface of the electrodes and consists of two parallel and opposing layers of charges surrounding the electrodes, and in Sabet et al. [84], a high rate of discharge was used for nickel, cobalt, and aluminum (NCA) batteries to study the effect of battery aging, the experimental results show that due to the growth and structural damage of the cathode SEI layer is less in the high frequency region, but the impedance is still increasing in the mid-frequency region, which is due to the decomposition of the cathode SEI layer and the formation of the cathode–electrolyte interface (CEI) film at the anode–electrolyte interface.

The impedance magnitude in the mid-frequency range is influenced by the depletion of the cathode's active material, which encompasses the double-layer capacitance and charge transfer resistance at the interface between the battery electrodes and the electrolyte.

This interaction generates a double-layer effect when ions adsorb onto the electrode surfaces, resulting in two parallel and opposing charge layers surrounding the electrodes. Sabet et al. proposed a high discharge rate employed for NCA batteries to investigate the impact of battery aging [84]. The experimental findings indicate that, despite the reduced growth and structural damage of the cathode SEI layer in the high-frequency region, impedance continues to rise in the mid-frequency region due to the decomposition of the cathode SEI layer and the formation of the cathode–electrolyte interface film at the anode–electrolyte interface.

The EIS-based SOH estimation method is defined in terms of capacity and internal resistance from a selection of characteristic parameters with different performances, as follows [12]:

$$SOH = \frac{C_{now}}{C_0}100\%, \tag{13}$$

$$SOH = \frac{R_{EOL} - R_{now}}{R_{EOL} - R_{new}}100\%, \tag{14}$$

where $C_{now}$ represents the maximum permissible discharge capacity, $C_0$ signifies the standard capacity of the battery, $R_{now}$ indicates the internal resistance at the present moment, $R_{new}$ refers to the internal resistance of a new battery, and $R_{EOL}$ denotes the internal resistance after the battery's lifespan. Zhang et al. propose a battery model that utilizes charge transfer resistance, temperature, and SOC as input variables, leveraging the advantages of EIS [85]. The study examines the effects of ambient temperature, SOC, and battery aging on impedance spectra through EIS modeling, extracting charge transfer resistance for SOH estimation. A data-driven methodology can be employed to assess the battery health condition, thereby circumventing the intricacies of modeling by concentrating on the extraction of SOH-related information from extensive datasets [86]. Pradyumna et al. utilized a convolutional neural network to analyze EIS data. Subsequently, they assessed the cycle life of a lithium battery using a fully connected neural network, illustrating that the cycle life of lithium batteries can be evaluated through neural network analysis of the impedance behavior of multiple batteries to comprehend the aging patterns of the battery [87].

In summary, although the SOH of Li-ion batteries affects the impedance spectrum over the full frequency range, the aging of Li-ion batteries is more prominently affected by factors such as the electrolyte and the SEI layer. Battery aging is manifested in the form of the growth of the SEI layer and the decomposition of the electrolyte, which in turn leads to the growth of the battery ohmic impedance. The impedance spectrum of medium frequency, high frequency, and ultra-high frequency is seriously sensitive to the above factors, so the prediction of SOH for lithium batteries can be analyzed using the ohmic impedance of EIS. In recent years, some researchers have also used non-linearities to analyse the aging pattern of batteries, using odd random phase multi-frequency sinusoidal to three-electrode experimental battery experiments, proving that there is a correlation between the change of non-linearities and the aging pattern of the batteries, which provides a new way of thinking for the researchers so that they can better quantify the causes of the aging of the batteries [54,55].

### 5.2. Charge State Estimation

The impedance spectrum is intricately connected to the internal reaction mechanism of the battery. When a perturbing current is applied to the battery, the battery system exhibits varying reactions to different frequencies of current or voltage, which can be associated with particular physical processes. Through qualitative analysis of the many resistive components, one may construct a model of the power supply system and then analyze the impedance across different frequencies, enabling the assessment of the battery's SOC using impedance spectra. The examination of a battery by impedance spectroscopy enables the battery to be The impedance spectrum analysis of the battery can distinguish the impacts of various internal components, allowing for the identification of the actual variables

influencing the SOC, hence facilitating the development of an estimation algorithm for SOC assessment [88].

Certain investigations indicate that high-frequency and following partial medium-frequency impedances (100 Hz–10 kHz) exhibit minimal dependence on the relaxation time, although these impedances consistently vary with the states of the battery. This indicates the practicality of simultaneous estimation of SOC by employing the impedance within these ranges [89]. Battery impedance exhibits a more pronounced response to temperature and SOC in the low-frequency domain, facilitating the detection of these parameters. Conversely, its response is less distinct in the high-frequency domain, rendering the impedance characteristics across varying SOC states inadequately represented in that region [90]. Zhang et al. examined the mechanisms by which ambient temperature, state of charge, and battery aging affect the measured impedance of the battery by electrochemical impedance spectroscopy modeling [85,91]. Figure 8 illustrates that the initial arc is independent of SOC across all temperature scenarios, suggesting that the SEI layer does not influence SOC. Furthermore, it suggests that the charge transfer resistance, represented by the subsequent arc, impacts SOC. The figure illustrates that the second impedance arc diminishes and subsequently grows when the SOC declines at low temperatures. A comparable relationship is evident at 40 °C; however, it requires the amplification of the combined first and second impedance arcs for observation. Referring to [92], the correlation between charge transfer resistance Rct and SOC was measured, as shown in Equation (15).

$$R_{ct} \propto (SOC(1 - SOC))^{-1/2}. \tag{15}$$

Wang et al. examined the influence of SOC and temperature on circuit parameters, specifically analyzing the impact of cell SOC on ohmic resistance, charge transfer resistance, and Warburg impedance at varying temperatures [93]. The findings indicated that the sensitivity of ohmic resistance and charge transfer resistance to SOC is inferior to that of temperature. Conversely, Warburg impedance, as illustrated in Figure 9, was observed within the 10–95% SOC range, with Warburg resistance typically diminishing as temperature increases. In the lowest SOC range of 0–5%, Warbug resistance exhibits a sudden increase at elevated temperatures of 293 K and 303 K, whereas it demonstrates a sudden increase across all temperatures in the greatest SOC range of 95–100%. The potential cause for this phenomenon is that the buildup of lithium ions at the cathode and anode during discharge and charging markedly diminishes the diffusion rate of solid-state lithium ions, particularly at extreme states of charge, resulting in an escalation of Warburg resistance. In summary, the influence of SOC on Warburg resistance surpasses that of ohmic resistance and charge transfer resistance, so Warburg impedance can be utilized as a metric to estimate the SOC of lithium-ion batteries.

In conclusion, although there is a strong correlation between the internal resistance of Li-ion batteries and their SOC, SOC estimation can be accomplished by describing the relationship characterized by perturbation signals. However, most of the existing studies for the estimation of the SOC of Li-ion batteries are dominated by the use of equivalent circuits, whose parameters are determined by impedance measurements, and the prediction of the SOC of Li-ion batteries is achieved by using impedance components or correlations between specific frequencies and themselves. The main reason that impedance spectra are seldom utilized for the direct estimation of battery SOC is due to the fact that unlike temperature and SOH, SOC does not respond as sensitively to impedance spectra in the mid- and high-frequency regions as temperature and SOH. In the low-frequency region, impedance spectra are more affected, and the cost of using impedance to detect battery SOC is high.
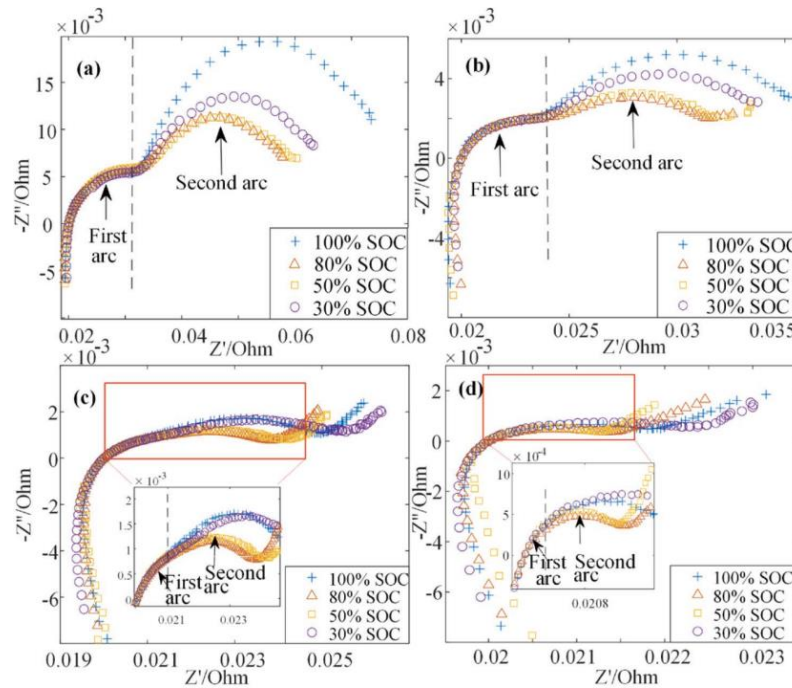
**Figure 8.** Impedance spectrum of four cells at different SOC levels after 400 aging cycles. (**a**) 10 °C, (**b**) 25 °C, (**c**) 40 °C, (**d**) 55 °C [85].
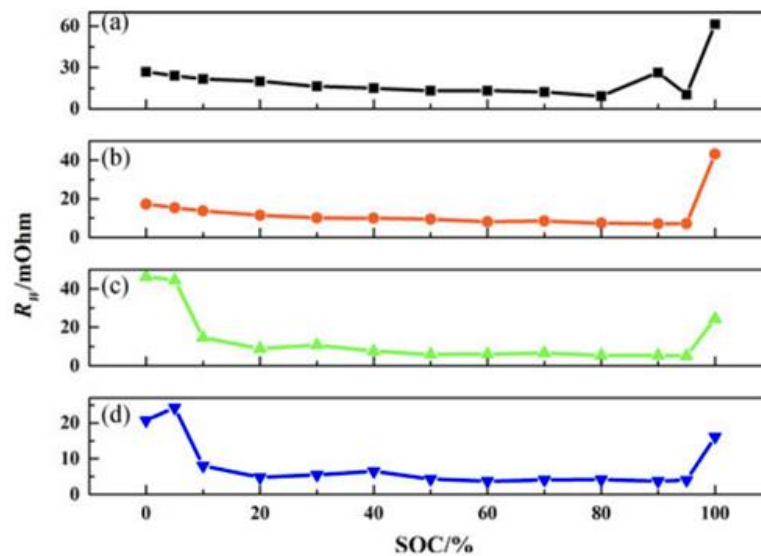


**Figure 9.** Warburg resistance profiles with respect to SOC at different temperatures: (**a**) 273 K, (**b**) 283 K, (**c**) 293 K, and (**d**) 303 K [93].

In recent years, the application of machine learning to lithium batteries has evolved to better help researchers understand the relationship between SOC and EIS while improving the accuracy of the models. Buchicchio et al. [94] proposed a SOC estimation method based on EIS and equivalent circuit models to provide a compact approach to describe the frequency and time domain behavior of the battery impedance. The proposed method allows very efficient model training and generates a low-dimensional SOC classification model with an accuracy of more than 93 %. It is confirmed that EIS data can distinguish between different states of charge with good reliability. A new idea is provided for online SOC estimation of batteries.

### 5.3. Battery Fault Diagnosis

Ensuring the safe operation of Li-ion batteries is crucial; otherwise, they may suffer performance deterioration and thermal runaway, potentially resulting in severe repercussions. Prevalent lithium battery faults encompass overcharge, overdischarge, lithium precipitation, internal short circuits, and thermal runaway [5,95].

Figure 10 illustrates the surface temperature, voltage, and dynamic impedance of a pouch battery subjected to overcharging conditions, which indicates that overcharging introduces excessive energy to the battery, alters its impedance, and results in overheating, potentially leading to accidents [96]. While overdischarge is less hazardous than short-circuiting and over-charging, it nonetheless impacts the battery's lifespan; recurrent overdischarge may result in a permanent decrease in battery capacity and hasten the decline of battery performance [97]. Furthermore, lithium plating is a critical concern regarding battery aging and safety. This phenomenon typically transpires during the charging process of lithium batteries, where lithium ions deposit on the surface of the lithium metal within the anode materials. Ideally, this lithium metal should reintegrate into the redox reaction; however, a significant portion transforms into 'dead lithium,' leading to diminished capacity. In more severe instances, lithium dendrites form, causing a permanent decline in battery capacity and hastening the degradation of battery performance [97]. In extreme instances, lithium dendrites form, compromising the battery's safety [98]. The examination of impedance spectra provides critical insights into failure mechanisms, aiding in the differentiation between normal and abnormal batteries, hence mitigating the danger of premature failure.
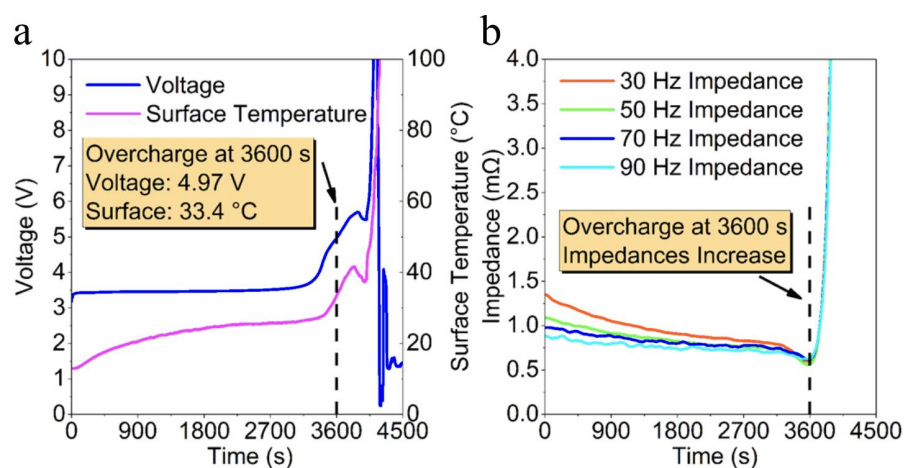


**Figure 10.** The charging process starts at 0 s, and the overcharge starts at 3600 s, as indicated by the arrow. (**a**) shows the voltage and surface temperature $T_{surf}$ variation, and (**b**) shows the dynamic impedances of multiple frequencies.[96].

As demonstrated in Section 2, the impedance in the high-frequency domain correlates with the decomposition of the electrolyte and the development of the SEI film on the electrode material [22]. Furthermore, the impedance in this domain is minimally influenced by extraneous variables such as the SOC levels and load current, thereby facilitating the identification of overcharging and discharging issues in batteries. Prolonged overdischarge results in numerous irreversible alterations, including copper dissolution [8], increased impedance [99], and decomposition of the SEI layer [100], subsequently precipitating the thermal runaway of the battery.

Currently, multisine-based perturbation signal is regarded as a method for monitoring individual cells in Li-ion battery packs; however, its practical application is hindered by space and power constraints. Carkhuff et al. introduced a compact, low-power battery management system utilizing multi-frequency (1–1000 Hz) impedance measurements to address the aforementioned issues by monitoring and analyzing mismatches and tempera-

ture abnormalities in each cell [101]. Discrepancies and other thermal irregularities arise, particularly during battery charging, discharging, and idle states, to guarantee battery safety and efficacy. Thermal runaway resulting from overcharging can be prevented by monitoring impedance during overcharging incidents.

The mid-frequency impedance spectrum is predominantly constrained by charge transfer and exhibits heightened sensitivity to temperature, hence serving as a detection parameter for thermal runaway. Lyu et al. conducted experiments on battery overcharging [96]. The results, illustrated in Figure 11, indicate that at the onset of overcharging, the slope of the dynamic impedance in the frequency range of 30–90 Hz transitions from negative to positive. It is noted that the impedance spectra of overcharged batteries differ from those of normally operating batteries. Furthermore, the 70 Hz impedance is pointed out as an example of preventing thermal runaway by disconnecting power when the slope shifts from negative to positive during charging. Consequently, the impedance parameter inside this frequency domain may serve as an early detection indicator for thermal runaway, and the perturbation signal must position the characteristic frequency inside the designated frequency range.
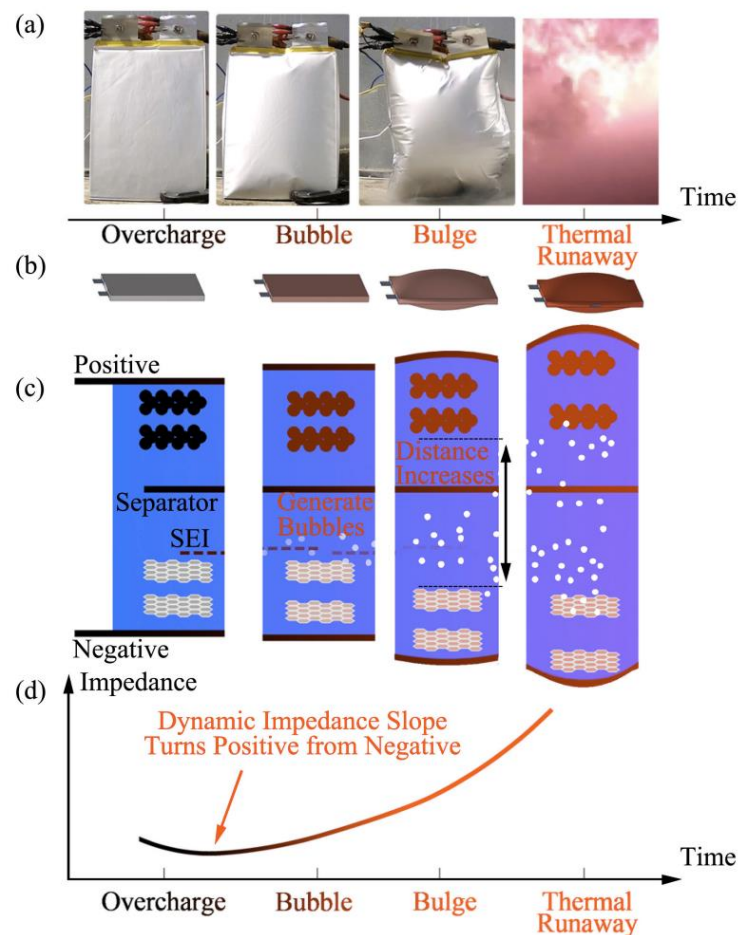


**Figure 11.** Schematic diagram of the LIB that demonstrates the feature that impedance slope turns positive from negative when the cell starts to overcharge. (**a**) Optical picture of the cell at different stages during overcharge. (**b**) Shape schematic of the cell at different stages. (**c**) Theoretical explanations on impedance increasing with bubbles and bulges. (**d**) Expected impedance curve during overcharge [96].

The low-frequency impedance is primarily influenced by the diffusion processes of lithium ions in both solid and liquid phases. This diffusion phenomenon characterizes the movement of charged and uncharged particles to equilibrate the concentration gradient

induced by variations in electrochemical potential, thus serving as a detection parameter for lithium precipitation. Schindler et al. conducted electrochemical impedance analysis during voltage relaxation, executed at 10 min intervals over one hour following the charging period [102]. They performed impedance measurements using a constant current, restricting the minimum test frequency to 0.5 Hz to maintain brevity in the impedance measurements, with the results illustrated in Figure 12. This posits that the recovery of these two resistance values correlates with the depletion of live lithium on the anode surface. Koseoglou et al. suggested a method for detecting lithium precipitation utilizing dynamic electrochemical impedance spectroscopy for the impedance analysis of lithium-ion batteries [103]. The low-frequency impedance dummy component of the battery is monitored in real time by superimposing sinusoidal currents onto the charging current. The emergence of a valley characteristic point in the low-frequency impedance dummy component during the initial charging phase signifies lithium precipitation.
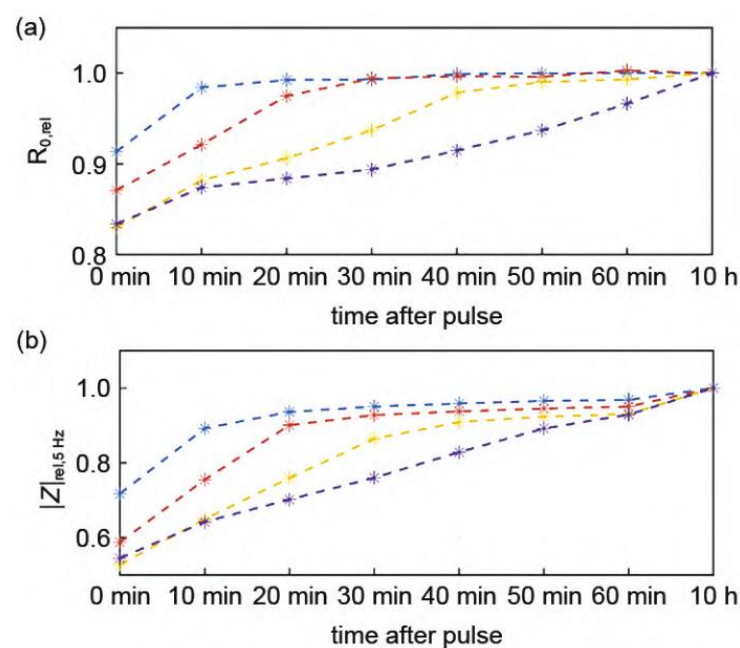


**Figure 12.** Experiments were conducted at ambient temperature $T = -15C$, initial $SOC = 50\%$, and charging current I = 2 C. A short impedance spectrum test plus a 10-h measurement was performed every 10 min for one hour after charging the battery to different SOC end states, with (**a**) $R_{0,rel}$ (the point with the imaginary part of 0) and (**b**) $|Z|_{rel,5Hz}$ (the frequency of the 5 Hz impedance real part) two resistance values with relaxation time (different colors represent different changing SOCs) [102].

*5.4. Battery Modeling*

To extend battery life and guarantee safe operation, it is imperative to develop a dependable battery management system that monitors the battery's condition, and the model-based algorithm for battery control and monitoring has been widely applied. Thus, an accurate battery mathematical model is required to ensure performance and acquire the battery parameters [104,105]. For onboard BMS applications, the equivalent circuit model (ECM), utilizing various fundamental circuit components such as voltage sources, resistors, and parallel configurations of resistor–capacitor combinations, is extensively utilized to simulate the current–voltage characteristics and transient responses of lithium-ion batteries [106], as shown in Figure 13.
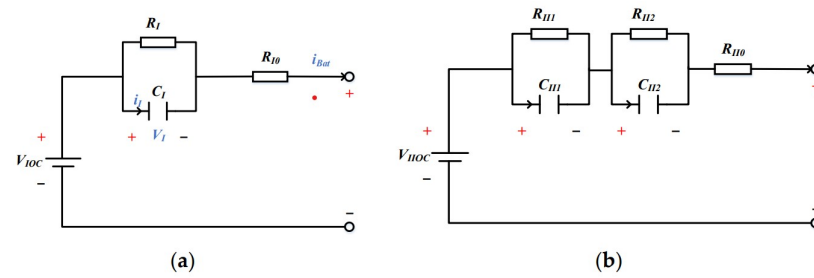
**Figure 13.** The examples of equivalent circuit models (ECM). (**a**) 1-RC circuit model; (**b**) 2-RC circuit model [107].

Battery impedance is predominantly determined by ohmic internal resistance, whereas polarization internal resistance displays significant variability relative to the SOC level [108]. To estimate the parameter of ECM impedance-related components, the square wave-based perturbation signal, termed the hybrid pulse power characterization method (HPPC), is employed to accurately measure the charging and discharging ohmic resistance and the polarization internal resistance [109]. The primary objective of this square wave signal is to evaluate the operational pulse power of the battery at various SOC levels, examine the correlation between the response voltage and current during charging, discharging, and resting phases, and compute the internal resistance [110]. An ECM can be developed to replicate the operational condition of the battery based on the voltage and current responses obtained from the HPPC test. The usual HPPC test current and voltage graphs are illustrated in Figure 14, and its calculation formula is provided as follows [111]:

$$R_0 = \frac{\triangle U_0}{I} = \frac{U_B - U_A}{I}, \tag{16}$$

$$R_p = \frac{\triangle U_p}{I} = \frac{U_C - U_B}{I}, \tag{17}$$

where $R_0$ denotes the ohmic internal resistance; $R_p$ signifies the polarization internal resistance; $I$ represents the current (A); $\triangle U_0$ indicates the voltage variation associated with the ohmic internal resistance (V); $\triangle U_p$ denotes the voltage variation corresponding to the polarization internal resistance (V); $U_A$ represents the initial voltage of the discharging work-step; $U_B$ denotes the final voltage of the discharging work-step; $U_C$ indicates the final voltage of the stationary work-step.
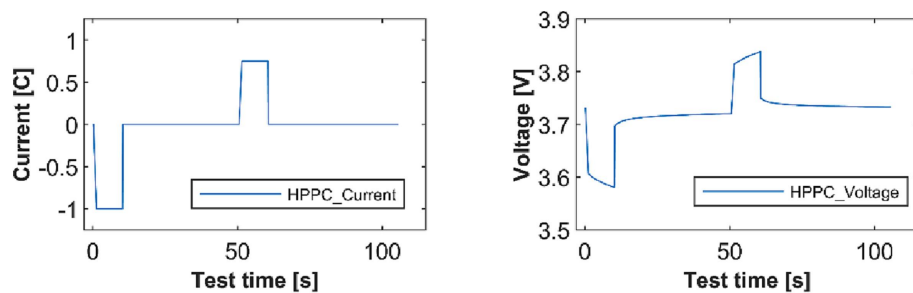


**Figure 14.** HPPC test based direct current (DC) pulse test current curve (**left**) and example voltage response (**right**) [111].

Like the square wave signal, the step signal has also been utilized in battery modeling. The internal resistance of the battery encompasses ohmic internal resistance, concentrated differential polarization internal resistance, and charge transfer internal resistance. Each type of internal resistance can indicate various states and power characteristics of the battery. The resistive and high-frequency regions correspond to impedance, whereas the impedance value in the mid-frequency region is dictated by the charge transfer process and double-layer capacitance [16]. Consequently, the internal resistance value in this frequency

range can be assessed using the step signal-based approach, termed direct current internal resistance test method (DCIR).

The DCIR is a prevalent method for assessing the DC internal resistance by utilizing the dynamic features of the battery, capitalizing on the stability of the battery's SOC following a brief alteration in the operating current. Pan et al. introduced a methodology for identifying the components of direct current internal resistance via both DC and alternating current internal resistance testing [112]. They employed the Butler–Volmer equation and a second-order ECM to simulate the time constants that characterize interfacial charge transfer and concentration polarization processes. Figure 15 illustrates that the final results of electrochemical polarization internal resistance identification exhibit a minimum error of under 5% compared to the electrochemical impedance test results and an average error of 3.7% to the EIS ohmic internal resistance test results, thereby confirming the method's reliability.
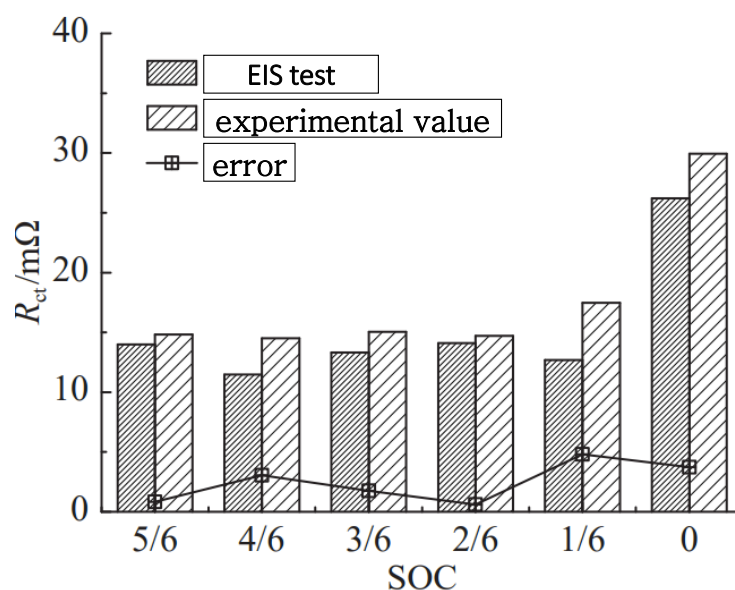


**Figure 15.** Comparison of cell polarization internal resistance impedance spectral values and experimental measurements and their errors [112].

While the DCIR test technique can effectively characterize and quantify ohmic internal resistance, charge transfer internal resistance, and polarization internal resistance, it proves challenging to differentiate between charge transfer internal resistance and ohmic internal resistance during actual measurements [113]. This difficulty arises because the diffusion rate of lithium ions within the battery is significantly slower than the interfacial charge transfer rate [114]. Typically, the interfacial charge transfer duration is considerably shorter than the DCIR sampling interval. Consequently, the instantaneous internal resistance associated with voltage fluctuations predominantly comprises ohmic internal resistance and polarization internal resistance. Therefore, to delineate the resistance associated with charge transfer for advanced battery modeling, a characterization method including a broadband frequency range should be contemplated.

The ECM necessitates great precision in its bandwidth, which should encompass the frequency range of the realistic driving cycle; hence, frequency domain battery models and associated characterization methods have garnered considerable interest. The sine-sweep-based signal, such as EIS, serves as the primary technique not only for analyzing and characterizing the electrochemical properties of lithium-ion batteries but also for battery modeling [115]. Figure 16 illustrates the LIB EIS plot alongside its fractional-order equivalent circuit model, which is segmented into three distinct regions: a low-frequency straight segment, a mid-frequency semi-circle segment, and a high-frequency segment, where the resistance R0 in the high-frequency region denotes the battery's ohmic resistance.

The mid-frequency curve is not a semicircle, indicating that the conventional RC network structure is inadequate for modeling the battery's characteristics in this frequency range; thus, a constant phase element (CPE) should be utilized in place of a capacitor. Additionally, a CPE that represents the properties of an imperfect double-layer capacitor has been employed to model the depressed semicircles in the Nyquist plots [116], thus leading to the proposal of a fractional order equivalent circuit model [117]. Yang et al. introduced a simplified fractional order impedance model employing a genetic method for parameter identification, achieving a voltage inaccuracy of less than 0.5% [118]. Mu et al. [119] and Xiong et al. [120] employed a fractional order equivalent circuit model and Kalman filtering to assess the state of charge and conduct reliability analysis of lithium batteries.

The low-frequency component pertains to the diffusion effect of the battery's positive and negative electrodes, represented by $Z_{FSW}$ for Warburg impedance. Figure 16 illustrates that the prevalent equivalent circuit elements for simulating diffusion behavior include finite space Warburg (FSW), finite length Warburg (FLW), and CPE [27]. The Randles model comprises an ohmic resistor, several resistors and capacitors arranged in parallel, and Warburg impedance, enabling the model to analyze and simulate large time-constant diffusion processes [121].
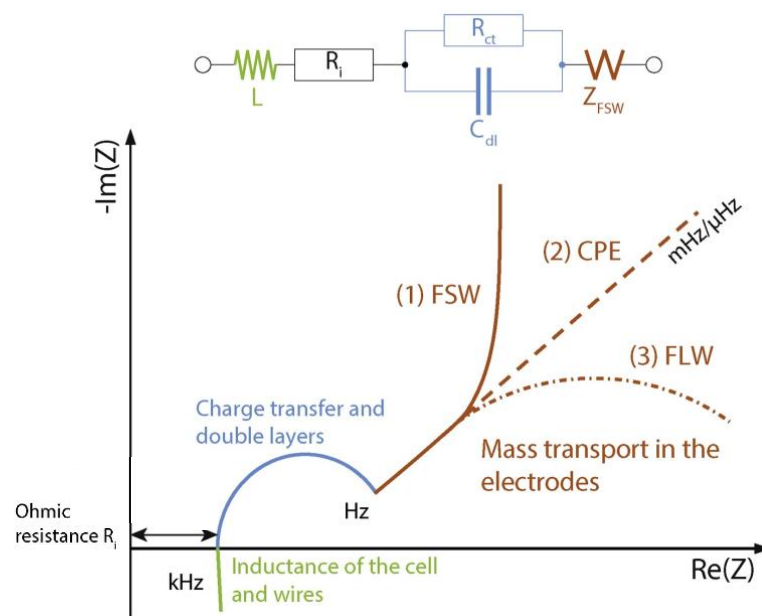


**Figure 16.** Typical impedance spectrum of a Li-ion cell and common EC to model the impedance behavior. Four different loss processes can be identified. The low frequency diffusion behavior is typically modeled by (1) a finite space Warburg, (2) a constant phase element, or (3) a finite length Warburg [27].

The frequency domain equivalent circuit model adopts the measured impedance data to fit the model parameters, which can more accurately describe the dynamic characteristics of the lithium-ion battery, and the model accuracy is higher than that of the conventional time domain ECM. Meanwhile, equivalent circuit models are now often used to detect the SOC and SOH of battery packs. The model-based approach to detecting the SOH of a battery is to consider the whole battery as one ECM or to consider each individual cell as one ECM and then connect each ECM to each other. For example, Bi et al. [122] established a second-order equivalent circuit model for resistive-capacitive circuits and optimized the state space of the model by combining it with a genetic resampling particle filter to improve the model accuracy. Finally, the study, in conjunction with real data, demonstrated better performance than the traditional particle filtering method. Diao et al. [123] found that there is a link between the maximum available energy (MAE) of the battery pack and the degradation and inconsistency of the battery pack, based on which

a first-order ECM model was developed, and the ECM was used to calculate the MAE of each individual cell to obtain the MAE of the whole battery pack. This method of using the MAE to study the aging of battery packs provides a new way of thinking for researchers. However, the method of detecting the SOH of lithium batteries using ECM will have a conflict between accuracy and computational effort. To solve the above problems, the researchers proposed to integrate battery pack SOH and inconsistency modeling to predict the SOH of the battery pack. The former is to divide the aging of the battery pack into the degradation of individual cells and the consistent degradation of the whole battery, model the inconsistency of different parameters of each individual cell in the aging of the battery, and compute the reversible loss due to the inconsistency to derive the MAE of the battery pack [124]. Figure 17 shows a specific flow chart. The latter is inconsistency modeling. In terms of inconsistency modeling, Xu et al. [125] performed SOH estimation for each battery and obtained the SOH difference by obtaining the voltage of each battery. Using the method of wavelet analysis, more detailed battery information can be obtained.
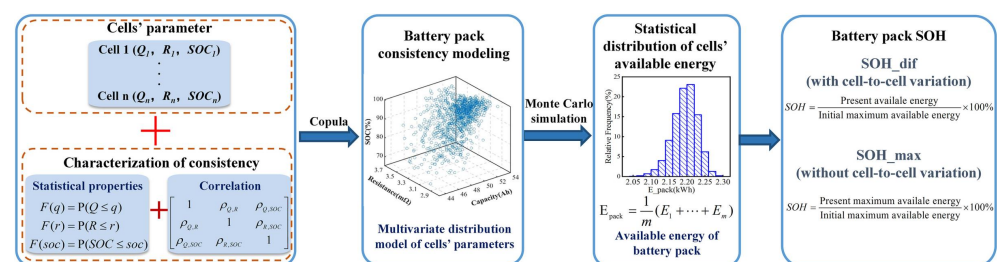


**Figure 17.** A scheme for battery pack state-of-health estimation based on the present (maximum) available energy [124].

For the detection of battery pack SOC, the current mainstream method is also predicted by modeling the battery pack. This method has high accuracy and reliability and is suitable for real-time applications [126]. For the detection of battery pack SOC, the current mainstream method is also predicted by modeling the battery pack. This method has high accuracy and reliability and is suitable for real-time applications. In practice, inconsistencies in the internal and external parameters of the battery can lead to inaccurate SOC measurements. These factors include differences in capacity, differences in internal resistance, and the way the battery is connected. Inconsistencies in internal parameters can be attributed to design and assembly factors. Differences in internal resistance can lead to higher currents between cells, resulting in capacity degradation [127]. In terms of battery connection methods, parallel and then series battery packs can better reduce the effects of variations in battery parameters and greatly increase the usable capacity and power of the battery packs [128]. In the case of the battery connection methods, parallel and then series battery packs can better reduce the effects of variations in battery parameters and greatly increase the usable capacity and power of the battery packs [129]. Xiong et al. [130] used capacity and impedance as indicators to establish a parametric battery model and used Adaptive Extended Kalman Filter to estimate the SOC, and the results showed that the SOC error of the battery pack was less than 2%. There are also researchers' methods to estimate the SOC for each unit in the battery. Chen et al. [131] built an ECM model consisting of an open circuit voltage source and a series RC network for each individual cell in the battery pack, and used Kalman Filter algorithm to estimate the SOC for each individual cell. The accuracy of this method is high, but when the number of cells is large, the computation is too large for the case. To improve the performance and reduce the inconsistency, some researchers have also proposed to let the first cell that reaches the cut-off voltage as a representative cell to estimate the SOC of the battery pack [132].

## 6. Discussion and Prospects

Currently, battery impedance has advanced considerably in evaluating the performance of electrochemical energy storage, safety monitoring, and battery management

system (BMS) design. Despite the utilization of numerous characterization approaches, including the innovative perturbation signals method, unresolved challenges persist as the onboard practical implementation for energy storage expands, and the expectations for safety, dependability, and capacity intensify. Future research priorities and development directions will concentrate on the following aspects:

(1) The impedance measurement process is vulnerable to interference from various factors, including noise and temperature. Additionally, the detection of internal resistance requires enhancement for onboard practical applications. Therefore, it is essential to investigate new testing methods and technologies, potentially integrating deep learning and neural network algorithms to enhance the identification of dynamic changes in impedance measurement.

(2) Regardless of the ability of contemporary mainstream perturbation signals to encompass measurements within the accessible frequency domain, each perturbation signal exhibits a blind spot in impedance measurement, preventing the comprehensive assessment of the entire frequency spectrum. Furthermore, each signal possesses inherent limitations; for instance, the pseudo-random sequence signal, while offering rapid measurement, suffers from a low signal-to-noise ratio in comparison to alternative signals. Consequently, comprehensive investigation and implementation of the signals are required.

(3) Further study is required on the impedance properties of batteries throughout various operating situations, particularly in the mid and low-frequency ranges, to facilitate improved battery modeling and more precise impedance measurements. The impedance measuring process should be streamlined, and more cost-effective and easily implementable methods must be developed to accommodate various regional settings and onboard application scenarios.

(4) As the energy storage industry continues to evolve, many new issues arise, such as volatility in the energy system and the tension between the energy supplier and the demand side [133]. The relationship between new energy systems and the power industry is becoming more and more intricate, with new connections being made in all sectors, and even more so between education and practice. In this interdisciplinary study of energy, the new field of energy informatics plays an important role. In order to solve problems, traditional energy science can be combined with the current new methods of machine learning [134]. Therefore, for lithium battery research, it is important to combine research, education, and practice for the development of energy informatics. Currently, many lithium battery impedance testing techniques can only be performed in the laboratory for economic reasons. Laboratories need specialists with skills related to managing and analysing complex data on batteries, the ability to address the challenges of future integrated energy systems and a good educational philosophy of energy informatics. When training students, researchers should focus not only on theoretical understanding but also on the development of practical skills [135]. In this way, researchers will be able to seize the opportunity to lead their research teams to success and break through the limitations of lithium battery testing technology from the laboratory to practical applications.

In summary, battery impedance measurement techniques will help sustain the new energy industry and popularize chemical power applications. Continuous research and innovation on battery impedance measurement methods, variables, applications, and measurement improvement by comprehensive evaluation of multiple factors, data sampling optimization, battery internal resistance database establishment, and machine learning technology make impedance measurement methods more advanced, accurate, and applicable to a variety of complex working conditions.

## 7. Conclusions

This paper discusses the main types of perturbation signals used to measure battery impedance and their respective advantages and disadvantages. The paper elucidates and

compares the precise composition of each type of perturbation signal, such as sinusoidal sweep signals, step signals, square wave signals, pseudo-random sequence signals, and multi-sine signals. The report also explores the advantages and disadvantages of each perturbation signal through theoretical and application evaluations. These signals can be affected by various external factors and other influences in practical applications, which can cause errors in the measurement results, so future research should enhance the reliability and stability of impedance measurements.

The factors affecting impedance measurements, such as signal-to-noise ratio, signal amplitude and power spectrum, are also analyzed. The emerging perturbation signals used for impedance measurement have some of the above problems and do not allow for accurate measurements over the full frequency band. When the perturbation signal amplitude is too large, the lithium battery will be non-linear. In order to improve the understanding of the impedance spectrum, some researchers have also launched a study on the non-linearity of the battery, hoping to extract the information containing the impedance spectrum from the non-linearity of the battery. The current research trend is to design a simple, efficient, accurate and cost-effective impedance testing technique for in-vehicle applications, and the signal generator and data acquisition device should be further optimized to be suitable for existing BMSs.

The applications of using perturbation signals to characterize battery impedance are reviewed, and the future prospects of impedance characterization methods are outlined. Also, this paper expresses that there are many intricate relationships between the battery impedance response and the internal chemical reaction mechanism and physical properties of Li-ion batteries, some parts of which are difficult to express. To solve the above-mentioned complexities, a more accurate battery impedance model should be developed. Batteries are affected by multiple factors such as temperature, SOC, and SOH coupling, and it is difficult to delineate the boundaries between the impedance characteristics of Li-ion battery impedance exhibited by different factors. Therefore, it is necessary to study and understand the correlation between different factors and impedance characteristics more deeply so that the interface between impedance changes caused by different factors can be more obvious.

This review establishes the theoretical framework of perturbation signals for onboard impedance characterization methods. Impedance spectra are also discussed with respect to their application to battery packs; this motivates researchers to further investigate and apply impedance spectroscopy as a reliable and effective tool for battery management and provides valuable insights for readers aiming to develop the optimal range of applications for battery BMS.

## References

1. Khan, F.; Rasul, M.; Sayem, A.; Mandal, N. Maximizing energy density of lithium-ion batteries for electric vehicles: A critical review. *Energy Rep.* **2023**, *9*, 11–21. [CrossRef]
2. Li, H.; Kaleem, M.B.; Liu, Z.; Wu, Y.; Liu, W.; Huang, Z. IoB: Internet-of-batteries for electric Vehicles–Architectures, opportunities, and challenges. *Green Energy Intell. Transp.* **2023**, *2*, 100128. [CrossRef]
3. Li, R.; Bao, L.; Chen, L.; Zha, C.; Dong, J.; Qi, N.; Tang, R.; Lu, Y.; Wang, M.; Huang, R.; et al. Accelerated aging of lithium-ion batteries: Bridging battery aging analysis and operational lifetime prediction. *Sci. Bull.* **2023**, *68*, 3055–3079. [CrossRef] [PubMed]
4. Nyamathulla, S.; Dhanamjayulu, C. A review of battery energy storage systems and advanced battery management system for different applications: Challenges and recommendations. *J. Energy Storage* **2024**, *86*, 111179. [CrossRef]
5. Sun, J.; Chen, S.; Xing, S.; Guo, Y.; Wang, S.; Wang, R.; Wu, Y.; Wu, X. A battery internal short circuit fault diagnosis method based on incremental capacity curves. *J. Power Sources* **2024**, *602*, 234381. [CrossRef]
6. Birkl, C.R.; Roberts, M.R.; McTurk, E.; Bruce, P.G.; Howey, D.A. Degradation diagnostics for lithium ion cells. *J. Power Sources* **2017**, *341*, 373–386. [CrossRef]
7. Ge, M.F.; Liu, Y.; Jiang, X.; Liu, J. A review on state of health estimations and remaining useful life prognostics of lithium-ion batteries. *Measurement* **2021**, *174*, 109057. [CrossRef]
8. Guo, R.; Lu, L.; Ouyang, M.; Feng, X. Mechanism of the entire overdischarge process and overdischarge-induced internal short circuit in lithium-ion batteries. *Sci. Rep.* **2016**, *6*, 30248. [CrossRef]
9. Osaka, T.; Mukoyama, D.; Nara, H. Development of diagnostic process for commercially available batteries, especially lithium ion battery, by electrochemical impedance spectroscopy. *J. Electrochem. Soc.* **2015**, *162*, A2529. [CrossRef]
10. Mc Carthy, K.; Gullapalli, H.; Ryan, K.M.; Kennedy, T. Use of impedance spectroscopy for the estimation of Li-ion battery state of charge, state of health and internal temperature. *J. Electrochem. Soc.* **2021**, *168*, 080517. [CrossRef]
11. Sun, X.; Zhang, Y.; Zhang, Y.; Wang, L.; Wang, K. Summary of health-state estimation of lithium-ion batteries based on electrochemical impedance spectroscopy. *Energies* **2023**, *16*, 5682. [CrossRef]
12. Liu, Y.; Wang, L.; Li, D.; Wang, K. State-of-health estimation of lithium-ion batteries based on electrochemical impedance spectroscopy: A review. *Prot. Control. Mod. Power Syst.* **2023**, *8*, 1–17. [CrossRef]
13. Choi, W.; Shin, H.C.; Kim, J.M.; Choi, J.Y.; Yoon, W.S. Modeling and applications of electrochemical impedance spectroscopy (EIS) for lithium-ion batteries. *J. Electrochem. Sci. Technol.* **2020**, *11*, 1–13. [CrossRef]
14. Habte, B.T.; Jiang, F. Effect of microstructure morphology on Li-ion battery graphite anode performance: Electrochemical impedance spectroscopy modeling and analysis. *Solid State Ionics* **2018**, *314*, 81–91. [CrossRef]
15. Zhang, W.; Li, T.; Wu, W.; Ouyang, N.; Huang, G. Data-driven state of health estimation in retired battery based on low and medium-frequency electrochemical impedance spectroscopy. *Measurement* **2023**, *211*, 112597. [CrossRef]
16. Du, X.; Meng, J.; Amirat, Y.; Gao, F.; Benbouzid, M. Exploring impedance spectrum for lithium-ion batteries diagnosis and prognosis: A comprehensive review. *J. Energy Chem.* **2024**, *94*, 464–483. [CrossRef]
17. Chen, L.; Lü, Z.; Lin, W.; Li, J.; Pan, H. A new state-of-health estimation method for lithium-ion batteries through the intrinsic relationship between ohmic internal resistance and capacity. *Measurement* **2018**, *116*, 586–595. [CrossRef]
18. Illig, J.; Ender, M.; Weber, A.; Ivers-Tiffée, E. Modeling graphite anodes with serial and transmission line models. *J. Power Sources* **2015**, *282*, 335–347. [CrossRef]
19. Matsuda, T.; Ando, K.; Myojin, M.; Matsumoto, M.; Sanada, T.; Takao, N.; Imai, H.; Imamura, D. Investigation of the influence of temperature on the degradation mechanism of commercial nickel manganese cobalt oxide-type lithium-ion cells during long-term cycle tests. *J. Energy Storage* **2019**, *21*, 665–671. [CrossRef]
20. Yoon, J.; Jang, S.; Choi, S.H.; Park, J.; Kim, K.H.; Park, H.S.; Jeong, S.; Kwon, S.; Woo, K.; Yang, W. Deciphering the degradation mechanism of thick graphite anodes in high-energy-density Li-ion batteries by electrochemical impedance spectroscopy. *J. Ind. Eng. Chem.* **2024**, *138*, 424–431. [CrossRef]
21. Song, J.; Lee, H.; Wang, Y.; Wan, C. Two-and three-electrode impedance spectroscopy of lithium-ion batteries. *J. Power Sources* **2002**, *111*, 255–267. [CrossRef]
22. Agubra, V.A.; Fergus, J.W. The formation and stability of the solid electrolyte interface on the graphite anode. *J. Power Sources* **2014**, *268*, 153–162. [CrossRef]
23. Zhang, S.; Andreas, N.S.; Li, R.; Zhang, N.; Sun, C.; Lu, D.; Gao, T.; Chen, L.; Fan, X. Mitigating irreversible capacity loss for higher-energy lithium batteries. *Energy Storage Mater.* **2022**, *48*, 44–73. [CrossRef]
24. Eddahech, A.; Briat, O.; Woirgard, E.; Vinassa, J.M. Remaining useful life prediction of lithium batteries in calendar ageing for automotive applications. *Microelectron. Reliab.* **2012**, *52*, 2438–2442. [CrossRef]
25. Baert, D.H.; Vervaet, A. A new method for the measurement of the double layer capacitance for the estimation of battery capacity. In Proceedings of the 25th International Telecommunications Energy Conference, Yokohama, Japan, 23 October 2003; pp. 733–738.
26. Macdonald, J.R.; Johnson, W.B.; Raistrick, I.; Franceschetti, D.; Wagner, N.; McKubre, M.; Macdonald, D.; Sayers, B.; Bonanos, N.; Steele, B.; et al. *Impedance Spectroscopy: Theory, Experiment, and Applications*; John Wiley & Sons: Hoboken, NJ, USA, 2018.
27. Oldenburger, M.; Beduerftig, B.; Gruhle, A.; Grimsmann, F.; Richter, E.; Findeisen, R.; Hintennach, A. Investigation of the low frequency Warburg impedance of Li-ion cells by frequency domain measurements. *J. Energy Storage* **2019**, *21*, 272–280. [CrossRef]
28. Fan, C.; Liu, K.; Ren, Y.; Peng, Q. Characterization and identification towards dynamic-based electrical modeling of lithium-ion batteries. *J. Energy Chem.* **2024**, *92*, 738–758. [CrossRef]

29. Dam, S.K.; John, V. High-resolution converter for battery impedance spectroscopy. *IEEE Trans. Ind. Appl.* **2017**, *54*, 1502–1512. [CrossRef]

30. Wei, X.; Wang, X.; Dai, H. Practical on-board measurement of lithium ion battery impedance based on distributed voltage and current sampling. *Energies* **2018**, *11*, 64. [CrossRef]

31. Kallel, A.Y.; Kanoun, O. On the design of multisine signals for maintaining stability condition in impedance spectroscopy measurements of batteries. *J. Energy Storage* **2023**, *58*, 106267. [CrossRef]

32. Tang, X.; Lai, X.; Liu, Q.; Zheng, Y.; Zhou, Y.; Ma, Y.; Gao, F. Predicting battery impedance spectra from 10-s pulse tests under 10 Hz sampling rate. *IScience* **2023**, *26*, 106821. [CrossRef]

33. Gabrielli, C.; Huet, F.; Keddam, M.; Lizee, J. Measurement time versus accuracy trade-off analyzed for electrochemical impedance measurements by means of sine, white noise and step signals. *J. Electroanal. Chem. Interfacial Electrochem.* **1982**, *138*, 201–208. [CrossRef]

34. Su, X.; Sun, B.; Wang, J.; Zhang, W.; Ma, S.; He, X.; Ruan, H. Fast capacity estimation for lithium-ion battery based on online identification of low-frequency electrochemical impedance spectroscopy and Gaussian process regression. *Appl. Energy* **2022**, *322*, 119516. [CrossRef]

35. Hoshi, Y.; Yakabe, N.; Isobe, K.; Saito, T.; Shitanda, I.; Itagaki, M. Wavelet transformation to determine impedance spectra of lithium-ion rechargeable battery. *J. Power Sources* **2016**, *315*, 351–358. [CrossRef]

36. Itagaki, M.; Ueno, M.; Hoshi, Y.; Shitanda, I. Simultaneous determination of electrochemical impedance of lithium-ion rechargeable batteries with measurement of charge-discharge curves by wavelet transformation. *Electrochim. Acta* **2017**, *235*, 384–389. [CrossRef]

37. Wang, X.; Kou, Y.; Wang, B.; Jiang, Z.; Wei, X.; Dai, H. Fast calculation of broadband battery impedance spectra based on S transform of step disturbance and response. *IEEE Trans. Transp. Electrif.* **2022**, *8*, 3659–3672. [CrossRef]

38. Yokoshima, T.; Mukoyama, D.; Nakazawa, K.; Gima, Y.; Isawa, H.; Nara, H.; Momma, T.; Osaka, T. Application of electrochemical impedance spectroscopy to ferri/ferrocyanide redox couple and lithium ion battery systems using a square wave as signal input. *Electrochim. Acta* **2015**, *180*, 922–928. [CrossRef]

39. Yokoshima, T.; Mukoyama, D.; Nara, H.; Maeda, S.; Nakazawa, K.; Momma, T.; Osaka, T. Impedance measurements of kilowatt-class lithium ion battery modules/cubicles in energy storage systems by square-current electrochemical impedance spectroscopy. *Electrochim. Acta* **2017**, *246*, 800–811. [CrossRef]

40. Wang, L.; Song, Z.; Zhu, L.; Jiang, J. Fast electrochemical impedance spectroscopy of lithium-ion batteries based on the large square wave excitation signal. *IScience* **2023**, *26*, 106463. [CrossRef]

41. Yao, Q.; Lu, D.; Lei, G. Battery impedance measurement using fast square current perturbation. In Proceedings of the 4th International Future Energy Electronics Conference (IFEEC), Singapore, 24–28 November 2019; pp. 1–5.

42. Meng, J.; Peng, J.; Cai, L.; Song, Z. Rapid impedance extraction for lithium-ion battery by integrating power spectrum and frequency property. *IEEE Trans. Ind. Electron.* **2023**, *10*, 112. [CrossRef]

43. Du, X.; Meng, J.; Peng, J.; Liu, Y. A novel lithium-ion battery impedance fast measurement method with enhanced excitation signal. *IEEE Trans. Ind. Electron.* **2023**, *70*, 12322–12330. [CrossRef]

44. Tan, A.H.; Godfrey, K.R. The generation of binary and near-binary pseudo-random signals: An overview. In Proceedings of the 18th IEEE Instrumentation and Measurement Technology Conference (IMTC 2001), Budapest, Hungary, 21–23 May 2001; Volume 2, pp. 766–771.

45. Sihvo, J.; Stroe, D.I.; Messo, T.; Roinila, T. Fast approach for battery impedance identification using pseudo-random sequence signals. *IEEE Trans. Power Electron.* **2019**, *35*, 2548–2557. [CrossRef]

46. Liebhart, B.; Diehl, S.; Schneider, D.; Endisch, C.; Kennel, R. Enhancing the cell impedance estimation of a lithium-ion battery system with embedded power path switches. In Proceedings of the 2021 IEEE Applied Power Electronics Conference and Exposition (APEC), Phoenix, AZ, USA, 14–17 June 2021; pp. 967–974.

47. Schmidt, J.P. *Verfahren zur Charakterisierung und Modellierung von Lithium-Ionen Zellen*; KIT Scientific Publishing: Singapore, 2013; Volume 25.

48. Widanage, W.D.; Barai, A.; Chouchelamane, G.; Uddin, K.; McGordon, A.; Marco, J.; Jennings, P. Design and use of multisine signals for Li-ion battery equivalent circuit modelling. Part 2: Model estimation. *J. Power Sources* **2016**, *324*, 61–69. [CrossRef]

49. Yang, Y.; Zhang, F.; Tao, K.; Sanchez, B.; Wen, H.; Teng, Z. An improved crest factor minimization algorithm to synthesize multisines with arbitrary spectrum. *Physiol. Meas.* **2015**, *36*, 895. [CrossRef] [PubMed]

50. Janeiro, F.M.; Hu, Y.; Ramos, P.M. Peak factor optimization of multi-harmonic signals using artificial bee colony algorithm. *Measurement* **2020**, *150*, 107040. [CrossRef]

51. Horner, A.; Beauchamp, J. A genetic algorithm-based method for synthesis of low peak amplitude signals. *J. Acoust. Soc. Am.* **1996**, *99*, 433–443. [CrossRef]

52. Firouz, Y.; Relan, R.; Timmermans, J.; Omar, N.; Van Den Bossche, P.; Van Mierlo, J. Advanced lithium ion battery modeling and nonlinear analysis based on robust method in frequency domain: Nonlinear characterization and non-parametric modeling. *Energy* **2016**, *106*, 602–617. [CrossRef]

53. Fan, C.; O'regan, K.; Li, L.; Kendrick, E.; Widanage, W.D. Frequency domain non-linear characterization and analysis of lithium-ion battery electrodes. *J. Energy Storage* **2021**, *36*, 102371. [CrossRef]

54. Fan, C.; Grandjean, T.R.; O'Regan, K.; Kendrick, E.; Widanage, W.D. Understanding non-linearity in electrochemical systems using multisine-based non-linear characterization. In *Transactions of the Institute of Measurement and Control*; SAGE Publications Sage UK: London, UK, 2021; p. 01423312211045991.

55. Fan, C.; Liu, K.; Zhu, T.; Peng, Q. Understanding of Lithium-ion battery degradation using multisine-based nonlinear characterization method. *Energy* **2024**, *290*, 130230. [CrossRef]

56. Kallel, A.Y.; Kanoun, O. Crest factor optimization for multisine excitation signals with logarithmic frequency distribution based on a hybrid stochastic-deterministic optimization algorithm. *Batteries* **2022**, *8*, 176. [CrossRef]

57. Andre, D.; Meiler, M.; Steiner, K.; Wimmer, C.; Soczka-Guth, T.; Sauer, D. Characterization of high-power lithium-ion batteries by electrochemical impedance spectroscopy. I. Experimental investigation. *J. Power Sources* **2011**, *196*, 5334–5341. [CrossRef]

58. Gaberscek, M.; Dominko, R.; Jamnik, J. The meaning of impedance measurements of LiFePO$_4$ cathodes: A linearity study. *J. Power Sources* **2007**, *174*, 944–948. [CrossRef]

59. Huang, R.; Wang, X.; Jiang, B.; Chen, S.; Zhang, G.; Zhu, J.; Wei, X.; Dai, H. Revealing the electrochemical impedance characteristics of lithium-ion battery (nickel-cobalt-aluminum vs. graphite) under various alternating current amplitudes. *J. Power Sources* **2023**, *566*, 232929. [CrossRef]

60. Du, X.; Meng, J.; Peng, J. Hybrid pseudorandom sequence for broadband impedance measurements of lithium-ion batteries. *IEEE Trans. Ind. Electron.* **2022**, *70*, 6856–6864. [CrossRef]

61. Qahouq, J.A.A.; Xia, Z. Single-perturbation-cycle online battery impedance spectrum measurement method with closed-loop control of power converter. *IEEE Trans. Ind. Electron.* **2017**, *64*, 7019–7029. [CrossRef]

62. Peng, J.; Meng, J.; Du, X.; Cai, L.; Stroe, D.I. A fast impedance measurement method for lithium-ion battery using power spectrum property. *IEEE Trans. Ind. Inform.* **2022**, *19*, 8253–8261. [CrossRef]

63. Wünsch, M.; Füßler, R.; Sauer, D.U. Metrological examination of an impedance model for a porous electrode in cyclic aging using a 3-electrode lithium-ion cell with NMC111 | Graphite. *J. Energy Storage* **2018**, *20*, 196–203. [CrossRef]

64. Lee, P.K.; Tahmasebi, M.H.; Ran, S.; Boles, S.T.; Yu, D.Y. Leveraging titanium to enable silicon anodes in lithium-ion batteries. *Small* **2018**, *14*, 1802051. [CrossRef]

65. Sinha, N.N.; Burns, J.; Sanderson, R.; Dahn, J. Comparative studies of hardware corrosion at high potentials in coin-type cells with non aqueous electrolytes. *J. Electrochem. Soc.* **2011**, *158*, A1400. [CrossRef]

66. Belt, J.R.; Bernardi, D.M.; Utgikar, V. Development and use of a lithium-metal reference electrode in aging studies of lithium-ion batteries. *J. Electrochem. Soc.* **2014**, *161*, A1116. [CrossRef]

67. Jones, J.P.; Smart, M.C.; Krause, F.C.; Ratnakumar, B.V.; Brandon, E.J. The effect of electrolyte composition on lithium plating during low temperature charging of Li-ion cells. *ECS Trans.* **2017**, *75*, 1. [CrossRef]

68. Bard, A.J.; Inzelt, G.; Scholz, F. *Electrochemical Dictionary*; Springer: New York, NY, USA, 2012.

69. Delacourt, C.; Ridgway, P.L.; Srinivasan, V.; Battaglia, V. Measurements and simulations of electrochemical impedance spectroscopy of a three-electrode coin cell design for Li-Ion cell testing. *J. Electrochem. Soc.* **2014**, *161*, A1253. [CrossRef]

70. Wang, R.; Zhou, X.; Wang, Y.; Xiao, Y.; Shi, Z.; Liu, Y.; Zhang, T. Degradation analysis of lithium-ion batteries under ultrahigh-rate discharge profile. *Appl. Energy* **2024**, *376*, 124241. [CrossRef]

71. Li, Y.; Guo, W.; Stroe, D.I.; Zhao, H.; Kristensen, P.K.; Jensen, L.R.; Pedersen, K.; Gurevich, L. Evolution of aging mechanisms and performance degradation of lithium-ion battery from moderate to severe capacity loss scenarios. *Chem. Eng. J.* **2024**, *498*, 155588. [CrossRef]

72. Wang, L.; Zhao, X.; Deng, Z.; Yang, L. Application of electrochemical impedance spectroscopy in battery management system: State of charge estimation for aging batteries. *J. Energy Storage* **2023**, *57*, 106275. [CrossRef]

73. Sun, Y.; Xiong, R.; Wang, C.; Tian, J.; Li, H. Deep neural network based battery impedance spectrum prediction using only impedance at characteristic frequencies. *J. Power Sources* **2023**, *580*, 233414. [CrossRef]

74. Liang, K.; Zhang, Z.; Liu, P.; Wang, Z.; Jiang, S. Data-driven ohmic resistance estimation of battery packs for electric vehicles. *Energies* **2019**, *12*, 4772. [CrossRef]

75. Yoshida, T.; Takahashi, M.; Morikawa, S.; Ihara, C.; Katsukawa, H.; Shiratsuchi, T.; Yamaki, J.i. Degradation mechanism and life prediction of lithium-ion batteries. *J. Electrochem. Soc.* **2006**, *153*, A576. [CrossRef]

76. Schindler, S.; Danzer, M.A. A novel mechanistic modeling framework for analysis of electrode balancing and degradation modes in commercial lithium-ion cells. *J. Power Sources* **2017**, *343*, 226–236. [CrossRef]

77. Kassem, M.; Delacourt, C. Postmortem analysis of calendar-aged graphite/LiFePO4 cells. *J. Power Sources* **2013**, *235*, 159–171. [CrossRef]

78. Witt, D.; Röder, F.; Krewer, U. Analysis of Lithium-Ion Battery State and Degradation via Physicochemical Cell and SEI Modeling. *Batter. Supercaps* **2022**, *5*, e202200067. [CrossRef]

79. Bao, M.; Liu, D.; Wu, Y.; Wang, Z.; Yang, J.; Lan, L.; Ru, Q. Interpretable machine learning prediction for li-ion battery's state of health based on electrochemical impedance spectroscopy and temporal features. *Electrochim. Acta* **2024**, *494*, 144449. [CrossRef]

80. Wang, Y.C.; Chen, K.C. Classification of aged batteries based on capacity and/or resistance through machine learning models with aging features as input: A comparative study. *J. Clean. Prod.* **2024**, *471*, 143431. [CrossRef]

81. Aykol, M.; Gopal, C.B.; Anapolsky, A.; Herring, P.K.; van Vlijmen, B.; Berliner, M.D.; Bazant, M.Z.; Braatz, R.D.; Chueh, W.C.; Storey, B.D. Perspective—Combining physics and machine learning to predict battery lifetime. *J. Electrochem. Soc.* **2021**, *168*, 030525. [CrossRef]

82. Roman, D.; Saxena, S.; Robu, V.; Pecht, M.; Flynn, D. Machine learning pipeline for battery state-of-health estimation. *Nat. Mach. Intell.* **2021**, *3*, 447–456. [CrossRef]

83. Ng, M.F.; Zhao, J.; Yan, Q.; Conduit, G.J.; Seh, Z.W. Predicting the state of charge and health of batteries using data-driven machine learning. *Nat. Mach. Intell.* **2020**, *2*, 161–170. [CrossRef]

84. Sabet, P.S.; Warnecke, A.J.; Meier, F.; Witzenhausen, H.; Martinez-Laserna, E.; Sauer, D.U. Non-invasive yet separate investigation of anode/cathode degradation of lithium-ion batteries (nickel–cobalt–manganese vs. graphite) due to accelerated aging. *J. Power Sources* **2020**, *449*, 227369. [CrossRef]

85. Zhang, Q.; Huang, C.G.; Li, H.; Feng, G.; Peng, W. Electrochemical impedance spectroscopy based state-of-health estimation for lithium-ion battery considering temperature and state-of-charge effect. *IEEE Trans. Transp. Electrif.* **2022**, *8*, 4633–4645. [CrossRef]

86. Jiang, B.; Zhu, J.; Wang, X.; Wei, X.; Shang, W.; Dai, H. A comparative study of different features extracted from electrochemical impedance spectroscopy in state of health estimation for lithium-ion batteries. *Appl. Energy* **2022**, *322*, 119502. [CrossRef]

87. Pradyumna, T.; Cho, K.; Kim, M.; Choi, W. Capacity estimation of lithium-ion batteries using convolutional neural network and impedance spectra. *J. Power Electron.* **2022**, *22*, 850–858. [CrossRef]

88. Vadhva, P.; Hu, J.; Johnson, M.J.; Stocker, R.; Braglia, M.; Brett, D.J.; Rettie, A.J. Electrochemical impedance spectroscopy for all-solid-state batteries: Theory, methods and future outlook. *ChemElectroChem* **2021**, *8*, 1930–1947. [CrossRef]

89. Su, T.F.; Chen, K.C. Rapid monitor of states of lithium-ion batteries through non-quasi-static electrochemical impedance spectroscopy and terminal voltage. *J. Power Sources* **2023**, *586*, 233641. [CrossRef]

90. Gasper, P.; Schiek, A.; Smith, K.; Shimonishi, Y.; Yoshida, S. Predicting battery capacity from impedance at varying temperature and state of charge using machine learning. *Cell Rep. Phys. Sci.* **2022**, *3*, 101184. [CrossRef]

91. Fu, Z.; Sun, B.; Gong, J.; Gong, M.; Zhao, X.; Ma, S. A SOC Estimation Method for Li-Ion Batteries under High-Rate Pulse Conditions based on AO-BPNN Model. *Space Sci. Technol.* **2023**, *3*, 0088. [CrossRef]

92. Tian, J.; Xiong, R.; Shen, W. State-of-health estimation based on differential temperature for lithium ion batteries. *IEEE Trans. Power Electron.* **2020**, *35*, 10363–10373. [CrossRef]

93. Wang, Q.K.; He, Y.J.; Shen, J.N.; Hu, X.S.; Ma, Z.F. State of charge-dependent polynomial equivalent circuit modeling for electrochemical impedance spectroscopy of lithium-ion batteries. *IEEE Trans. Power Electron.* **2017**, *33*, 8449–8460. [CrossRef]

94. Buchicchio, E.; De Angelis, A.; Santoni, F.; Carbone, P.; Bianconi, F.; Smeraldi, F. Battery SOC estimation from EIS data based on machine learning and equivalent circuit model. *Energy* **2023**, *283*, 128461. [CrossRef]

95. McKerracher, R.D.; Guzman-Guemez, J.; Wills, R.G.; Sharkh, S.M.; Kramer, D. Advances in prevention of thermal runaway in Lithium-Ion batteries. *Adv. Energy Sustain. Res.* **2021**, *2*, 2000059. [CrossRef]

96. Lyu, N.; Jin, Y.; Xiong, R.; Miao, S.; Gao, J. Real-time overcharge warning and early thermal runaway prediction of Li-ion battery by online impedance measurement. *IEEE Trans. Ind. Electron.* **2021**, *69*, 1929–1936. [CrossRef]

97. Gan, N.; Sun, Z.; Zhang, Z.; Xu, S.; Liu, P.; Qin, Z. Data-driven fault diagnosis of lithium-ion battery overdischarge in electric vehicles. *IEEE Trans. Power Electron.* **2021**, *37*, 4575–4588. [CrossRef]

98. Gao, X.; Zhou, Y.N.; Han, D.; Zhou, J.; Zhou, D.; Tang, W.; Goodenough, J.B. Thermodynamic understanding of Li-dendrite formation. *Joule* **2020**, *4*, 1864–1879. [CrossRef]

99. Zhang, J.; Lee, J. A review on prognostics and health monitoring of Li-ion battery. *J. Power Sources* **2011**, *196*, 6007–6014. [CrossRef]

100. Fear, C.; Juarez-Robles, D.; Jeevarajan, J.A.; Mukherjee, P.P. Elucidating copper dissolution phenomenon in Li-ion cells under overdischarge extremes. *J. Electrochem. Soc.* **2018**, *165*, A1639–A1647. [CrossRef]

101. Carkhuff, B.G.; Demirev, P.A.; Srinivasan, R. Impedance-based battery management system for safety monitoring of lithium-ion batteries. *IEEE Trans. Ind. Electron.* **2018**, *65*, 6497–6504. [CrossRef]

102. Schindler, S.; Bauer, M.; Petzl, M.; Danzer, M.A. Voltage relaxation and impedance spectroscopy as in-operando methods for the detection of lithium plating on graphitic anodes in commercial lithium-ion cells. *J. Power Sources* **2016**, *304*, 170–180. [CrossRef]

103. Koseoglou, M.; Tsioumas, E.; Ferentinou, D.; Jabbour, N.; Papagiannis, D.; Mademlis, C. Lithium plating detection using dynamic electrochemical impedance spectroscopy in lithium-ion batteries. *J. Power Sources* **2021**, *512*, 230508. [CrossRef]

104. Ouyang, Q.; Chen, J.; Zheng, J. State-of-charge observer design for batteries with online model parameter identification: A robust approach. *IEEE Trans. Power Electron.* **2019**, *35*, 5820–5831. [CrossRef]

105. Fan, C.; O'Regan, K.; Li, L.; Higgins, M.D.; Kendrick, E.; Widanage, W.D. Data-driven identification of lithium-ion batteries: A nonlinear equivalent circuit model with diffusion dynamics. *Appl. Energy* **2022**, *321*, 119336. [CrossRef]

106. Shen, M.; Gao, Q. A review on battery management system from the modeling efforts to its multiapplication and integration. *Int. J. Energy Res.* **2019**, *43*, 5042–5075. [CrossRef]

107. Zhang, H.; Deng, C.; Zong, Y.; Zuo, Q.; Guo, H.; Song, S.; Jiang, L. Effect of sample interval on the parameter identification results of RC equivalent circuit models of li-ion battery: An investigation based on HPPC test data. *Batteries* **2022**, *9*, 1. [CrossRef]

108. Saghafi, M.; Chinnathambi, S.; Lemay, S.G. High-frequency phenomena and electrochemical impedance spectroscopy at nanoelectrodes. *Curr. Opin. Colloid Interface Sci.* **2023**, *63*, 101654. [CrossRef]

109. Cho, I.H.; Lee, P.Y.; Kim, J.H. Analysis of the effect of the variable charging current control method on cycle life of Li-ion batteries. *Energies* **2019**, *12*, 3023. [CrossRef]

110. Johnson, V. Battery performance models in ADVISOR. *J. Power Sources* **2002**, *110*, 321–329. [CrossRef]

111. Sun, J.; Kainz, J. Optimization of hybrid pulse power characterization profile for equivalent circuit model parameter identification of Li-ion battery based on Taguchi method. *J. Energy Storage* **2023**, *70*, 108034. [CrossRef]

112. Pan, B.; Dong, D.; Qian, D.; Niu, S.; Liu, S.; Jiang, Y. Quick identification of internal resistance components for lithium ion battery with LiFePO4. *J. Zhejiang Univ. Sci.* **2021**, *55*, 189–194.
113. Remmlinger, J.; Buchholz, M.; Meiler, M.; Bernreuter, P.; Dietmayer, K. State-of-health monitoring of lithium-ion batteries in electric vehicles by on-board internal resistance estimation. *J. Power Sources* **2011**, *196*, 5357–5363. [CrossRef]
114. Wang, Z.X.; Lu, Y.; Zhao, C.Z.; Huang, W.Z.; Huang, X.Y.; Kong, W.J.; Li, L.X.; Wang, Z.Y.; Yuan, H.; Huang, J.Q.; et al. Suppressing Li voids in all-solid-state lithium metal batteries through Li diffusion regulation. *Joule* **2024**, *8*, 2794–2810. [CrossRef]
115. Hallemans, N.; Howey, D.; Battistel, A.; Saniee, N.F.; Scarpioni, F.; Wouters, B.; La Mantia, F.; Hubin, A.; Widanage, W.D.; Lataire, J. Electrochemical impedance spectroscopy beyond linearity and stationarity—A critical review. *Electrochim. Acta* **2023**, 142939. [CrossRef]
116. Córdoba-Torres, P. Relationship between constant-phase element (CPE) parameters and physical properties of films with a distributed resistivity. *Electrochimica Acta* **2017**, *225*, 592–604. [CrossRef]
117. Wang, Y.; Tian, J.; Sun, Z.; Wang, L.; Xu, R.; Li, M.; Chen, Z. A comprehensive review of battery modeling and state estimation approaches for advanced battery management systems. *Renew. Sustain. Energy Rev.* **2020**, *131*, 110015. [CrossRef]
118. Yang, Q.; Xu, J.; Cao, B.; Li, X. A simplified fractional order impedance model and parameter identification method for lithium-ion batteries. *PLoS ONE* **2017**, *12*, e0172424. [CrossRef] [PubMed]
119. Mu, H.; Xiong, R.; Zheng, H.; Chang, Y.; Chen, Z. A novel fractional order model based state-of-charge estimation method for lithium-ion battery. *Appl. Energy* **2017**, *207*, 384–393. [CrossRef]
120. Xiong, R.; Tian, J.; Shen, W.; Sun, F. A novel fractional order model for state of charge estimation in lithium ion batteries. *IEEE Trans. Veh. Technol.* **2018**, *68*, 4130–4139. [CrossRef]
121. Li, A.G.; Mayilvahanan, K.; West, A.C.; Preindl, M. Discrete-time modeling of li-ion batteries with electrochemical overpotentials including diffusion. *J. Power Sources* **2021**, *500*, 229991. [CrossRef]
122. Bi, J.; Zhang, T.; Yu, H.; Kang, Y. State-of-health estimation of lithium-ion battery packs in electric vehicles based on genetic resampling particle filter. *Appl. Energy* **2016**, *182*, 558–568. [CrossRef]
123. Diao, W.; Jiang, J.; Zhang, C.; Liang, H.; Pecht, M. Energy state of health estimation for battery packs based on the degradation and inconsistency. *Energy Procedia* **2017**, *142*, 3578–3583. [CrossRef]
124. Yang, S.; Zhang, C.; Jiang, J.; Zhang, W.; Zhang, L.; Wang, Y. Review on state-of-health of lithium-ion batteries: Characterizations, estimations and applications. *J. Clean. Prod.* **2021**, *314*, 128015. [CrossRef]
125. Xu, J.; Mei, X.; Wang, X.; Fu, Y.; Zhao, Y.; Wang, J. A relative state of health estimation method based on wavelet analysis for lithium-ion battery cells. *IEEE Trans. Ind. Electron.* **2020**, *68*, 6973–6981. [CrossRef]
126. Sangeetha, E.; Subashini, N.; Santhosh, T.; Uma, D. Validation of EKF based SoC estimation using vehicle dynamic modelling for range prediction. *Electr. Power Syst. Res.* **2024**, *226*, 109905.
127. Hou, J.; Gao, T.; Yang, Y.; Wang, X.; Yang, Y.; Meng, S. Battery inconsistency evaluation based on hierarchical weight fusion and fuzzy comprehensive evaluation method. *J. Energy Storage* **2024**, *84*, 110878. [CrossRef]
128. Gogoana, R.; Pinson, M.B.; Bazant, M.Z.; Sarma, S.E. Internal resistance matching for parallel-connected lithium-ion cells and impacts on battery pack cycle life. *J. Power Sources* **2014**, *252*, 8–13. [CrossRef]
129. Luan, C.; Ma, C.; Wang, C.; Chang, L.; Xiao, L.; Yu, Z.; Li, H. Influence of the connection topology on the performance of lithium-ion battery pack under cell-to-cell parameters variations. *J. Energy Storage* **2021**, *41*, 102896. [CrossRef]
130. Xiong, R.; Sun, F.; Gong, X.; He, H. Adaptive state of charge estimator for lithium-ion cells series battery pack in electric vehicles. *J. Power Sources* **2013**, *242*, 699–713. [CrossRef]
131. Chen, Z.; Xia, B.; Mi, C.C. A novel state-of-charge estimation method for lithium-ion battery pack of electric vehicles. In Proceedings of the 2015 IEEE Transportation Electrification Conference and Expo (ITEC), Dearborn, MI, USA, 14–17 June 2015; pp. 1–6.
132. An, F.; Zhang, W.; Sun, B.; Jiang, J.; Fan, X. A novel state-of-energy simplified estimation method for lithium-ion battery pack based on prediction and representative cells. *J. Energy Storage* **2023**, *63*, 107083. [CrossRef]
133. Schmeck, H.; Monti, A.; Hagenmeyer, V. Energy informatics: Key elements for tomorrow's energy system. *Commun. ACM* **2022**, *65*, 58–63. [CrossRef]
134. Ling, C. A review of the recent progress in battery informatics. *NPJ Comput. Mater.* **2022**, *8*, 33. [CrossRef]
135. Bordin, C.; Mishra, S.; Safari, A.; Eliassen, F. Educating the energy informatics specialist: Opportunities and challenges in light of research and industrial trends. *SN Appl. Sci.* **2021**, *3*, 674. [CrossRef] [PubMed]